THESIS FOR THE DEGREE OF DOCTOR OF PHILOSOPHY

Spaceborne Synthetic Aperture Radar for Sea Ice Observations, Concentration and Dynamics

ANDERS BERG

Department of Earth and Space Sciences
CHALMERS UNIVERSITY OF TECHNOLOGY
Gothenburg, Sweden, 2014

Spaceborne Synthetic Aperture Radar for Sea Ice Observations, Concentration and Dynamics
ANDERS BERG
ISBN 978-91-7385-967-7

Doktorsavhandlingar vid Chalmers tekniska högskola
Ny serie Nr 3648
ISSN 0346-718X

Department of Earth and Space Sciences
Radar Remote Sensing Group
Chalmers University of Technology
SE-412 96 Gothenburg, Sweden
Telephone + 46 (0)31-772 1000

Cover:
Mean ice drift in the Fram Strait between April 2011 and April 2012, computed from 352 Envisat ASAR Wide Swath images.

Printed by Chalmers Reproservice
Chalmers University of Technology
Gothenburg, Sweden 2014

Vår position avgör vad vi ser
Ylva Eggehorn

Spaceborne Synthetic Aperture Radar for Sea Ice Observations, Concentration and Dynamics

ANDERS BERG
Department of Earth and Space Sciences
Chalmers University of Technology

ABSTRACT

Spaceborne Synthetic Aperture Radar (SAR) is the primary choice for sea ice monitoring due to its all-weather, day-and-night capability and regular delivery of high resolution images. This thesis presents methods for estimation of sea ice concentration and drift, a multi-sensor study of Baltic Sea ice radar signatures and an interferometric study of landfast sea ice. The ice concentration is determined by combining spatial autocorrelation and backscatter intensity in a neural network, which is trained with ice charts for the Baltic Sea. The root-mean-square error of the estimated concentration is found to be 7 percentage points for a spatially uniform distribution of ice concentrations. The ice drift is estimated from sequential SAR images by combining two methods: 1) areal matching by phase correlation, and 2) feature-based matching by detection and tracking of individual floes. The first method includes a module to resolve rotation. The second method is designed to assist tracking in the marginal ice zone and processes images in two steps: Firstly, by segmentation based on intensity thresholding to obtain objects corresponding to floes, and secondly, by feature tracking of floe outlines. A thresholding method that locates the antimode of imbalanced bimodal distributions is introduced, as well as a novel method for handling of aggregated floes. Assessment against manual measurements showed that up to 98% of drift vectors were estimated correctly, though the number varies with image pair and internal settings. Further, the ice drift algorithm is applied to C-band SAR images from a two-week spring period in the Fram Strait, and the measured ice drift is compared to drift modelled by the ice-ocean model HIROMB. The model is shown to overestimate the drift by a factor 1–2.5, attributable to an underestimated ice thickness, and to exhibit a 10°–30° offset in drift direction, independent of the drift direction. The thesis also evaluates the usefulness of spaceborne SAR sensors for ice charting. The traditionally employed C-band data is compared against X- and L-band data in terms of information content. It is found that L-band co-polarisation aids identification of ridge clusters and is less affected by microscale ice structures, whereas the information content in C- and X-band data is largely equivalent. Finally, interferometric acquisitions over landfast sea ice in the Bay of Bothnia demonstrate the capability of X-band SAR for small-scale deformation mapping of fast ice. Deformation occurs for example around leads, rocky islands and grounded ice ridges.

Keywords: sea ice concentration, sea ice dynamics, sea ice monitoring, satellite, synthetic aperture radar, interferometry

List of publications

Paper A

Berg, A. and L. E. B. Eriksson, SAR Algorithm for Sea Ice Concentration - Evaluation for the Baltic Sea. *IEEE Geoscience and Remote Sensing Letters.* vol. 9, no. 5, pp. 938–942, 2012

Paper B

Berg, A. and L. E. B. Eriksson, Investigation of a Hybrid Algorithm for Sea Ice Drift Measurements using Synthetic Aperture Radar Images. *IEEE Transactions on Geoscience and Remote Sensing,* in press.

Paper C

Berg, A., L. Axell and L. E. B. Eriksson, Comparison between SAR derived sea ice displacement and hindcasts by the operational ocean model HIROMB. Accepted for publication in *Proceedings of the IEEE International Geoscience and Remote Sensing Symposium*, Melbourne, Australia, July 21–26, 2013

Paper D

Eriksson, L. E. B., K. Borenäs, W. Dierking, A. Berg, M. Santoro, P. Pemberton, H. Lindh, and B. Karlson, Evaluation of new spaceborne SAR sensors for sea-ice monitoring in the Baltic Sea. *Canadian Journal of Remote Sensing.* vol. 36, suppl. 1, pp. S56–S73, 2010

Paper E

Berg, A., P. Dammert and L. E. B. Eriksson, X-Band Interferometric SAR Observations of Baltic Fast Ice. Submitted to *IEEE Transactions on Geoscience and Remote Sensing*

Acknowledgements

First and foremost, I would like to thank my supervisors Leif Eriksson and Lars Ulander for all their guidance and support. Without them this thesis would not exist. I am also deeply grateful to my assistant supervisor Wolfgang Dierking, for his willingly shared and rich expertise and research insight. I would like to express my gratitude to Karin Borenäs, for following me throughout my doctoral studies. Working with you has been a pleasure. I am deeply thankful to Patrik Dammert for his scientific advice and for devoting his spare time to assist me. I would also like to acknowledge Lars Axell, who has been a great collaborator.

I am thankful to my colleagues in the radar group, for all your encouragement and friendliness: Maciej, my tireless sounding board and travel companion, Gisela, Anatolii, Annelie, Gustaf, Jan, Janne, Malin, and Erik. I would like to thank all other people at the department for making it a pleasant working place, especially Donal, Mattias, Johan, and Marston. In addition, I would like to give thanks to all my floorball friends, for making Wednesday lunches a pleasant time. Thanks also to Johan at DTU, Thomas at AWI, and the people at SMHI and NPI that I have collaborated with.

Finally, I would like to thank my family for all their love and support.

Anders
Gothenburg, January 2014

Contents

1 Introduction **1**

1.1 Sea ice monitoring . . . 3

1.2 Radar remote sensing . . . 5

1.2.1 Basic principles . . . 5

1.3 Synthetic Aperture Radar . . . 7

1.3.1 Basic principle . . . 7

1.3.2 Ambiguity considerations in spaceborne SAR . . . 11

1.3.3 Interferometric SAR . . . 12

2 Radar backscatter from sea ice **17**

2.1 Physical properties of sea ice . . . 17

2.2 Surface and volume scattering . . . 18

2.3 SAR polarimetry and sea ice . . . 20

3 Material and methods **23**

3.1 SAR data . . . 23

3.1.1 Envisat . . . 24

3.1.2 ALOS . . . 25

3.1.3 TerraSAR-X . . . 26

3.1.4 COSMO-SkyMed . . . 26

3.1.5 RADARSAT-2 . . . 26

3.2 Field measurements . . . 26

3.3 Ancillary data . . . 27

4 Retrieval of ice parameters **29**

4.1 Sea ice concentration . . . 29

4.2 Sea ice drift . . . 30

5 Sea ice modelling **35**

5.1 Basic model elements . . . 35

5.1.1 Momentum balance 36
5.1.2 Conservation of ice mass 37
5.2 The HIROMB model 38

6 Summary of appended papers **41**
6.1 Paper A 41
6.2 Paper B 42
6.3 Paper C 42
6.4 Paper D 43
6.5 Paper E 43

7 Conclusion and future research **45**

Chapter 1

Introduction

Starting with Roald Amundsen's flight over the North Pole in the airship *Norge* in May 1926, the exploration of the Arctic region from above has carried on for almost a century. Today, the Arctic is commonly observed from much higher altitudes by polar orbiting satellites. These spacecrafts pass the northern ocean several times a day and provide detailed measurements of sea ice. The remote sensing technology has effectively been used to gain insight into the conditions of the Arctic sea ice cover and contributed to the development of a whole new research field.

Sea ice plays an important role in climatology. Acting as an insulator between the ocean water and the atmosphere, the ice cover regulates the heat exchange between the ocean and the air. Sea ice has an albedo higher than of the ocean and thereby reflects more of the incoming solar radiation. The fractional ice coverage is therefore affecting the amount of heat influx to the ocean. If the ice fraction decreases, more heat energy is stored in the surface water and consequently speeds up the melting. If, on the other hand, the ice fraction increases, more radiation is reflected which leads to more cooling. This effect is known as the sea ice-albedo feedback mechanism and is a crucial factor in explaining the long-term trend of declining Arctic sea ice seen over the last decades.

The climate change and diminishing ice poses a serious threat to the inhabitants of the harsh, polar environment. These inhabitants include not only the native Inuit people and large warm-blooded animals such as polar bears, birds and seals, but also many smaller organisms such as algae, worms and crustaceans. The Inuit rely on sea ice for harvesting of resources and travel. They must now adapt to later and slower freeze-up, more dynamic winter sea ice, and earlier and faster break-up [1]. The implications of these changes are considerable and involve enhanced travel danger and hampered access to hunting grounds. The traditionally hunted polar bear is at risk of losing its habitat which can lead to malnutrition and starvation. Bears are forced to swim longer distances, which cost them large amounts of energy and enhance the risk of drowning. The changing sea ice also affects the ability for the polar bears to build

proper dens.

The ice is also home to organisms further down in the food chain. An important example is the unicellular ice algae that forms in the lowermost sections of the ice and is food for zooplankton grazers. The peak production of the photosynthetic ice algae occurs in spring when the sun light returns [2]. At the same time, the solid ice cover starts to form individual floes and drift more freely, and the contents of the ice are spread to a wider area. The declining ice extent and new drift patterns may thus have a large impact on the marine ecosystems.

Sea ice change has implications also for the marine traffic in the polar region [3]. The major shipping lane known as the Northern Sea Route (or the Northeast Passage) is becoming more accessible and navigable as the melting season lasts longer. The new routes allow vessels to save large amounts of fuel compared to alternative routes through the Suez or the Panama Canal. Navigational support based on satellite imagery is essential for marine traffic in icy waters and radar imagery is the primary resource for ice analysts drawing charts of the ice conditions.

The first spaceborne microwave instrument useful for sea ice mapping was the Electrically Scanning Microwave Radiometer on board the Nimbus-5 satellite launched in 1972 [4]. The sensor measured the brightness temperature of horizontally polarised radiation emitted by the Earth and atmosphere system at a frequency of 19 GHz. At this frequency, sea ice can be distinguished from open water by its much higher emissivity. The spatial resolution provided by the radiometer was about 30 km [5]. The first Synthetic Aperture Radar (SAR) sensor which was used to map ice conditions from space was an L-band (1.3 GHz) radar carried on the U.S. Seasat satellite. This new sensor provided much finer resolution of $25\,\mathrm{m} \times 25\,\mathrm{m}$ at 4 looks. After the launch in 1978, the satellite did not operate for more than three months until it malfunctioned. Still, the Seasat mission was considered a technological and scientific success and effectively proved the usefulness of spaceborne SAR for sea ice monitoring [6, 7].

The objectives of this thesis are to present new methods for retrieval of sea ice concentration and sea ice drift using spaceborne SAR, to evaluate and compare the retrieval of these parameters against other data sets, to study the usefulness of recently launched SAR sensors for sea ice monitoring and to evaluate the potential of X-band SAR for landfast sea ice interferometry. The studied areas include the seasonally freezing Baltic Sea and the Fram Strait, located between Greenland and Svalbard, where ice is present year-round. The work carried out within the scope of this thesis have applications in climatology as well as for operational ice charting and ship routing, and may in a wider sense improve our understanding of sea ice dynamics.

The following chapters will provide a background to, and a summary of, the appended papers. The final part will give an outlook on the future and point towards areas of need for further research and development.

1.1 Sea ice monitoring

There are two main purposes of sea ice monitoring — to support marine traffic with navigational assistance and to monitor the environment, especially with focus on climate and climate change. While environmental studies have gained in importance in the recent years, ice charting has more than a century-long history.

Already in the 1890s, the Danish Meteorological Institute compiled ice charts over the Arctic region based on visual observations made by ship crews and observers on land [8]. These maps were produced monthly during the summer half-year and make a valuable source for research of historical ice conditions. As the technical development has proceeded, new sources of ice information have become available. One example is sonar measurements made from submarines, providing ice thickness along a transect. This type of measurements can also be made at fixed positions using bottom-anchored moorings equipped with upward looking sonars. In this case the very drift of the ice will produce the transect. Other sources of information include ice buoys, which are placed upon the ice to measure different ice properties such as ice temperature, thickness, growth and ablation, and movement using GPS. Ice buoys can also provide measurements of meteorological data such as atmospheric pressure, air temperature and surface winds. Sub-surface measurements of ocean currents and water temperature are made possible by buoys equipped with underwater sensors. Going on-shore, coastal radars can for instance be used to observe ice drift and evolution [9, 10].

Yet another method for ice monitoring is offered by aircrafts. Aerial reconnaissance has since long been used for making ice observations and, before the satellite era, it was the only substantial data source together with ship observations. Satellites have today replaced most of the duties that were performed with airborne platforms. Still observations and measurements from aircrafts are valuable and used for instance to gather validation data for the development of satellite-derived products.

Moving over to sea ice monitoring from space, there is a number of different types of instruments being used to study sea ice. These can broadly be divided in active microwave sensors such as SAR and scatterometers, passive microwave sensors, radar and laser altimeters and optical, infrared and near-infrared sensors. SAR sensors provide radar imagery in various frequency bands with a resolution down to one meter. Sea ice monitoring with SAR will be treated in depth in the following chapters. Passive microwave data have lower spatial resolution but provide larger spatial coverage. Typical values of the spatial resolution are 5–10 km and larger. Radar and laser altimeters are used to measure the sea ice freeboard, and indirectly, the ice thickness. Optical, infrared and near-infrared sensors are used for ice charting as a complement to other information sources. Further applications of infrared sensors include determination of thin ice thickness [11] and use of surface temperature data for numerical sea ice modelling [12].

Obviously there is a number of ice parameters that can be observed by spaceborne sen-

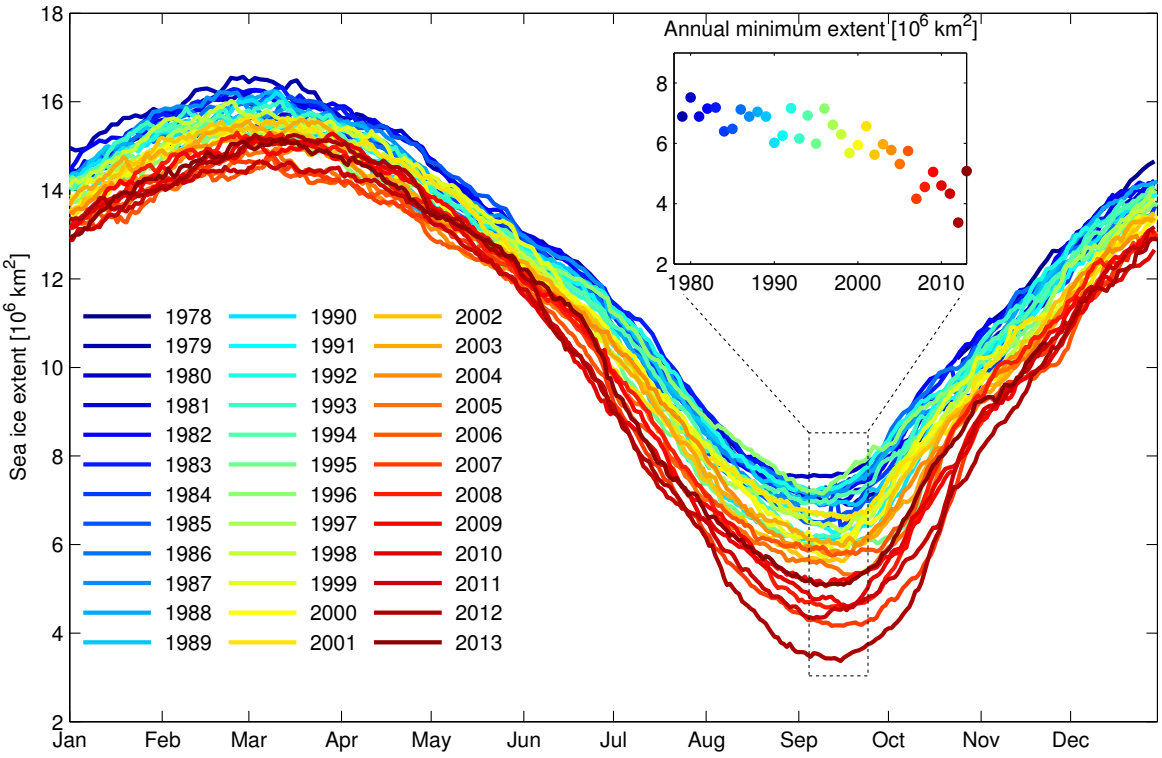

Figure 1.1: Daily sea ice extent and annual minimum extent at the Northern hemisphere, from 1978 to 2013, based on passive microwave data [14].

sors. One of the most fundamental observables is the sea ice extent, which specifies the sea area covered by ice to a certain fraction, usually set to 15 percent. Since the launch of the Nimbus-7 satellite in October 1978, the ice extent has been continuously monitored from space using passive microwave instruments. This time series of more than 35 years of sea ice extent has had great importance in climatology and been used to link changes in the cryosphere to anthropogenic forcings [13]. The measurements series is shown in figure 1.1, for the Northern hemisphere, along with the annual minimum extent which occurs every year in September.

Passive microwave sensors are also used to measure the ice concentration and the fractions of multi-year (MYI) and first-year ice (FYI) [15]. The microwave signature from the open ocean can be separated from that of sea ice by its larger difference between the vertically and horizontally polarised intensities. Ice concentration algorithms make use of the polarisation ratio, defined as the difference between the vertically and horizontally polarized radiances divided by their sum, as an ice/water discriminator. The polarisation ratio is nearly independent of the physical surface temperature which makes it a reliable measure [16]. The MYI can be separated from the FYI by the difference in brightness temperature between the 0.8 and 1.7 cm wavelengths, as the MYI exhibits a steeper gradient in brightness temperature. To measure the MYI

Table 1.1: Radar frequency bands

IEEE Standard Radar Band Nomenclature [18]		
Designation	Frequency	Wavelength
HF	3–30 MHz	100–10 m
VHF	30–300 MHz	10–1 m
UHF	300–1000 MHz	100–30 cm
L Band	1–2 GHz	30–15 cm
S Band	2–4 GHz	15–7.5 cm
C Band	4–8 GHz	7.5–3.75 cm
X Band	8–12 GHz	3.75–2.50 cm
K_u Band	12–18 GHz	2.50–1.67 cm
K Band	18–27 GHz	1.67–1.11 cm
K_a Band	27–40 GHz	1.11–0.75 cm
V Band	40–75 GHz	7.5–4.0 mm
W Band	75–110 GHz	4.0–2.7 mm
mm Band	110–300 GHz	2.7–1.0 mm

fraction, a spectral gradient ratio is formed, similar to the polarisation ratio. It is defined as the difference in vertically polarized radiances at the mentioned wavelengths, divided by their sum. The gradient ratio is dependent on the total ice fraction such that it is more sensitive to the MYI fraction at higher ice concentrations and loses all sensitivity over open water. It is also insensitive to variations in physical temperature in the same way as the polarisation ratio.

1.2 Radar remote sensing

1.2.1 Basic principles

A radar (**ra**dio **d**etection **a**nd **r**anging) is a device for transmission and reception of electromagnetic (EM) radiation that is reflected from some object. For a monostatic radar, the transmitting and receiving antenna is the same, as opposed to a bistatic radar. A radar system of the latter type has the transmitting and receiving antennas at two separate locations [17]. The range to an object is determined in case of a monostatic radar as the time delay of the signal multiplied by half the speed of light. The most fundamental property of a radar system is the frequency on which it operates. Table 1.1 lists the frequency bands used by radars together with their designations.

Polarisation

The radar may be designed to transmit the EM wave at a certain polarisation. The polarisation is defined from the direction of oscillation of the electric field component. Linear polarisation is most frequently used and can be either horizontal or vertical. If the radar receives the signal in the same polarisation as it was transmitted, the combination is referred to as co-polarisation. The alternative, cross-polarisation, uses orthogonal polarisations for transmission and reception. In this thesis we will use the abbreviations HH, HV, VH and VV for the horizontally (H) and vertically (V) polarized signals, where the first letter indicates the transmitted polarisation and the second letter indicates the received polarisation.

If H and V components are directed simultaneously to the antenna, with a phase offset of 90°, the polarisation is elliptical. If also the two components are equal in magnitude, the polarisation is circular. Circular polarisation is used for example by weather radars due to the high rain penetration. The two basis components of circular polarisation are denoted, based on the rotation sense, as left and right hand circular [19].

Resolution

The resolution of a radar system defines the ability of the radar system to separate two targets in close proximity. The range resolution depends on the properties of the radar pulse being transmitted. For an unmodulated pulse, the resolution is directly proportional to the pulse length. For a linear frequency modulated pulse, i.e. a chirp signal, utilization of matched filtering will improve the range resolution to [20]

$$\delta r = \frac{c}{2B}\,, \tag{1.1}$$

where c is the speed of light and B is the bandwidth of the transmitted signal. The ability of a scanning radar to separate targets at the same range is described by the angular resolution. Two targets can be resolved in angle if the angular separation is larger than the antenna beamwidth. The main lobe half power beamwidth is given by

$$\theta_B \approx \frac{\lambda}{D}\,, \tag{1.2}$$

where D is the size of the antenna aperture (e.g. diameter of dish antenna), λ is the wavelength and $\lambda \ll D$. For a rectangular shaped horn antenna, the radiation pattern from the wider side will be narrower than the radiation pattern from the narrow side.

There is also a third type of resolution that should be considered, which is the resolution in Doppler frequency. For a pulsed radar that illuminates two targets at the same range but with different range rates (i.e. time derivative of range), the targets can be resolved in Doppler frequency if the difference in range rate is larger than the resolution. The resolution is inversely

proportional to the dwell time, or the coherent pulse burst waveform duration. Better resolution is thus achieved by collecting input data a longer time, as it will generate more narrow peaks in the Doppler spectrum.

Received power and radar cross section

The amount of power being scattered back to the antenna is described by the following equation [21]:

$$S_{recd} = \frac{P_{trans} G^2 \lambda^2 \sigma}{(4\pi)^3 R^4 L_t L_{rad}^2 L_{ch}^2} \,. \tag{1.3}$$

Here P_{trans} is the transmitted power, G is the antenna gain, σ is the radar cross section of a target, R is the range to the target. L_t are losses in the microwave elements and transmission line, L_{rad} are losses in the antenna, and L_{ch} are losses in the atmosphere. The radar cross section is a key parameter. It is expressed in units of area and is a measure of the reflective strength of a target. Its value depends on the physical size and shape of the target, the materials of which the target is made, and the orientation of the target relative to the radar. Also the transmitted and received polarisation and the radar frequency have an impact on the radar cross section; the latter by the relative size of the target in relation to the wavelength.

It is convenient to normalize the radar cross section to surface area when the radar is measuring backscatter from a surface. The normalized radar cross section, or backscattering coefficient, is therefore given by [22]

$$\sigma^0 = \left\langle \frac{\sigma}{A} \right\rangle \,, \tag{1.4}$$

where σ is the total radar cross section of the contributing clutter[1] and A is the illuminated area.

1.3 Synthetic Aperture Radar

1.3.1 Basic principle

We have seen that for a real aperture radar, the resolution in the orthogonal, cross-range dimension is related to the antenna beamwidth. A synthetic aperture radar will produce much finer cross-range resolution by simulating a large array of antennas along the cross-range dimension and combine the contributions coherently.

[1] Regardless of its pejorative sense, the term clutter is widely used to denote echoes from land and sea surfaces.

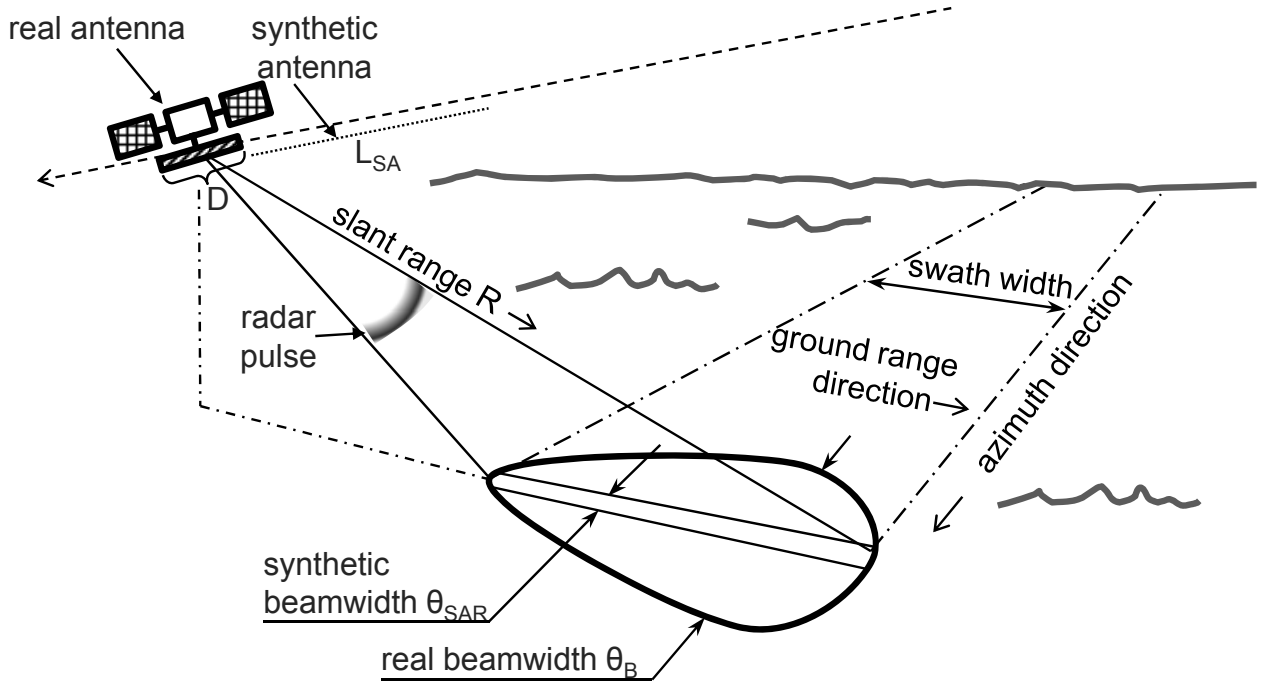

Figure 1.2: A synthetic aperture radar system sensing the sea surface. The azimuth direction is also referred to as cross-range.

Consider Fig. 1.2 in which a radar is moving along a path and observing an extended target. The recording device stores the complex radar return as function of range and antenna position into a two-dimensional matrix. The return from a stationary point scatterer will shift in phase as function of the antenna position, so that the scatterer appears to have a velocity along the radar line-of-sight. By taking the Fourier transform along each range bin in the two-dimensional data matrix, one will obtain Doppler spectra for all the range bins. The Doppler frequency is related to the position in azimuth direction, and in this way we have produced a two-dimensional, high-resolution image of the scene.

Note that the image processing technique described here is fairly crude, because the aim is to provide an intuitive understanding of the methodology. Usually it is preferred to apply more advanced algorithms to optimize the image quality. Specifically, it would be desirable to take into account migration of scatterers through range bins, and to consider non-linear phase functions. For more details, see for example [23].

The length of the synthetic aperture sets the limit on the resolution in the cross-range direction. If the synthetic aperture is made longer, it will increase the spatial bandwidth observed by the radar. A formula for the cross-range resolution can be inferred by regarding the synthetic aperture as a real aperture with length L_{SA}. Following Eq. (1.2), the antenna beamwidth becomes $\theta_{SAR} \approx \lambda/2L_{SA}$. The factor two in the denominator is due to the fact

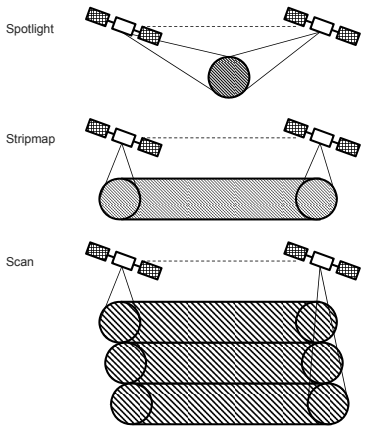

Figure 1.3: Three SAR modes: Spotlight SAR, stripmap and scanning mode. The satellite illuminates the shaded area on the ground as it passes over the scene.

that the signal is energized piecewise within the aperture, hence providing additional phase information as compared to a real aperture radar [24]. The synthetic antenna is thus twice as effective as a conventional antenna. At range R, the antenna beamwidth cover one resolution cell of length

$$\delta x = R \cdot \theta_{SAR} \approx \frac{R\lambda}{2L_{SA}} = \frac{\lambda}{2\theta_{int}} \tag{1.5}$$

in the cross-range direction, where θ_{int} is the integration angle, i.e. the angle subtended by the synthetic aperture. We can see that the cross-range resolution depends completely on the radar wavelength and the integration angle. Evidently, the integration angle is the key to obtaining fine cross-range resolution with SAR.

The SAR instrument may operate in different modes as illustrated by Fig. 1.3. Eq. (1.5) applies to all SAR modes, but a simplification can be made for stripmap SAR. In stripmap mode, the collection geometry is linear and the antenna is pointed to a fixed angle, normally broadside. In that case the integration angle and the beamwidth of the physical antenna are restricted by $\theta_{int} \leq \theta_B$. Eq. (1.5) then reduces to $\delta x \geq D/2$, which means that only the physical size of the antenna, D, determines the cross-range resolution. The resolution being independent of range makes SAR a useful instrument for spaceborne remote sensing.

In spotlight mode, the radar beam is continuously steered and pointed at the region of interest while the SAR passes over the scene. The purpose is to achieve wider integration angle θ_{int} and obtain finer spatial resolution in accordance with Eq. (1.5).

If it is desirable to image large areas, the primary choice would be to use scanning mode. In this mode, the radar beam is swept over several different subswaths. The subswaths are cyclically imaged by switching the antenna look angle. After the acquisition, each subswath

can be processed individually and radiometrically corrected before they are assembled [25]. A specific target within the scene will be illuminated a shorter time in comparison to stripmap mode. The length of the synthetic aperture, L_{SA}, will decrease respectively, and lead to coarser azimuth resolution [26].

A drawback of the ScanSAR acquisition scheme is the azimuth nonstationarity of the impulse response function [27]. Targets at different azimuths contribute with different central frequencies, due to different delays, and different amplitude weighting, due to the antenna pattern. The effects of these characteristics include a periodic amplitude modulation in azimuth and varying azimuth resolution. These problems of the ScanSAR mode can be eliminated by sweeping the radar beam in the azimuth direction, such that the beam is steered in an opposite way compared to the spotlight mode. This type of acquisition scheme will harmonize the performance in the along track direction. The imaging mode is known as TOPSAR and will be used by the forthcoming Sentinel-1 SAR satellite [28].

Speckle

Speckle is a noise-like quality characteristic of radar images and other images produced by coherent imaging systems such as lasers, sonars and ultrasound [29]. Speckle is not noise; it has its origin in a real electromagnetic measurement and is a property of the radar image itself. It is a consequence of the coherent summation of scattered fields from different scatterers within a resolution cell. Each scatterer contributes to the backscattered field with a phase and a magnitude change, such that the total returned modulation of the incident field is described by

$$Ae^{i\phi} = \sum_{k=1}^{N} A_k e^{i\phi_k} \,. \tag{1.6}$$

The summation is made over all illuminated scatterers. It may be understood from Eq. (1.6) that the speckle effect is due to interference effects caused by phase differences between scatterers. Scatterers in different parts of the resolution cell will typically contribute very different phase terms ϕ_k, considering that the slant range resolution span over many wavelengths. The distribution of phase terms ϕ_k can then be well described by a uniform distribution. The phase ϕ of the vector sum will also be uniformly distributed, and this is the source to the noise-like quality of the data.

Speckle can be reduced by multi-looking the SAR data. Multi-looking means that neighbouring image pixels are averaged noncoherently. This can for instance be realized by splitting the Doppler spectrum into L parts, and form one image from each part. The images can then be averaged incoherently to form a multi-looked image consisting of L looks. For single-look data, the intensity $I = A^2$ can be shown to have a negative exponential distribution [29]:

$$p_1(I) = \frac{1}{\sigma} \exp\left(-\frac{I}{\sigma}\right), \quad I \geq 0\,, \tag{1.7}$$

where σ is the total radar-cross-section of the targets within the resolution cell. σ is also the expectation value and the standard deviation of the intensity distribution. Forming an image by L independent looks will produce the following probability distribution:

$$p_L(I) = \frac{1}{\Gamma(L)} \left(\frac{L}{\sigma}\right)^L I^{L-1} \exp\left(-LI/\sigma\right), \quad I \geq 0 \tag{1.8}$$

For low values of L, the distribution is skewed with long positive tails, whereas the distribution will become similar to a normal distribution for high values of L. The expectation value after multi-looking will still be equal to σ, but the standard deviation is reduced to $\sigma/\sqrt{L}$.

1.3.2 Ambiguity considerations in spaceborne SAR

For unambiguous data recording, one must consider the sampling conditions. Ambiguities may arise in range as well as in azimuth. In the former case, the ambiguity is due to the periodic transmission of pulses. The time window used for reception of one pulse must not contain echoes from other pulses. Thus, the time extension of each echo must be smaller than the interval between two successive pulses. In addition, the radar echo should not arrive at the same time as the strong nadir echo to avoid distortions, nor should it arrive during transmission of a pulse since the receiver is blocked at that moment. These requirements limit the choice of pulse repetition frequency (PRF) to certain intervals, including an absolute upper limit [30].

The PRF must be further constrained in order to avoid azimuth ambiguities. Consider the fact that the recorded along-track phase function is weighted by the real aperture radiation pattern. The antenna pattern behaves just like a low-pass filter for broad-side collection, or band-pass filter for squinted collection [24]. The Doppler frequencies sampled by the SAR are aliased to some extent, because the filter formed by the antenna pattern does not have total out-of-band rejection. Increasing the PRF (or, equivalently, decreasing the along-track spacing of samples) reduces the amount of aliased energy into the sampled bandwidth of the Doppler frequency spectrum. If the along-track samples are spaced $\Delta_u \leq D/4$, the main lobe energy will not be subject to aliasing [31]. This sampling constraint may be relaxed somewhat, if the processed Doppler bandwidth is reduced (to some fraction of the sampled bandwidth) so that the majority of the aliased main lobe energy is excluded. The ratio of ambiguous target energy folded into the imaging processing bandwidth relative to the energy of the main signal within the processing bandwidth is known as the along-track ambiguity to signal ratio (AASR). This quantity is used to determine the level to which the PRF can be reduced.

To sum up, the PRF must be carefully chosen to balance the impacts of range and azimuth

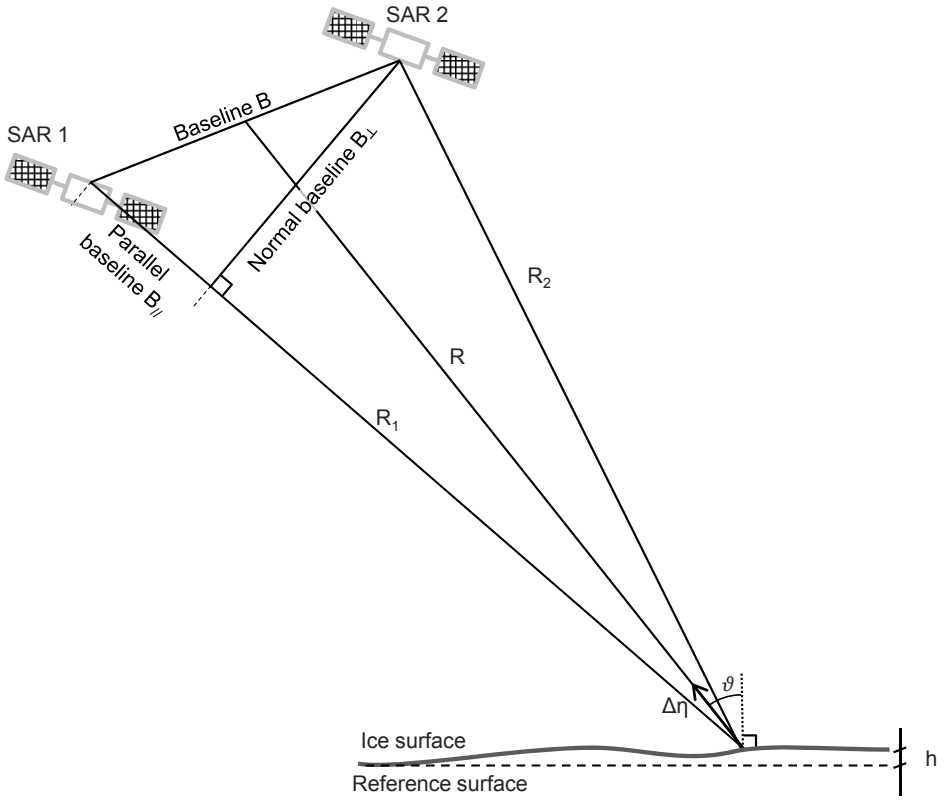

Figure 1.4: Geometry of a spaceborne repeat-pass interferometric SAR system. The figure is not according to scale.

ambiguities. This is more important to spaceborne SAR than for airborne systems due to the imaging geometry. First, the speed of the platform is much higher, which implies a much higher PRF. The high PRF together with the much longer distance to the scene means that multiple pulses are in flight at the same instant. To accomplish such a transmit scheme care must be taken so that the signal being received is not corrupted from adjacent echoes.

1.3.3 Interferometric SAR

Interferometric synthetic aperture radar (InSAR) is a technique to measure phase difference between coherent SAR images [32]. The use of InSAR for earth observation started in the mid 1980s, in the beginning using airborne SAR [33] and later on from satellite [34]. The information that can be retrieved with InSAR includes fine-scale surface deformation and ground elevation [35]. Two or more SAR images can be used, and these may be acquired on a single pass over the scene, using two separate antennas, or with repeated passes in the same orbit. For single-pass InSAR with two antennas mounted on the same platform, the antennas may be aligned in the across-track or along-track direction. Across-track mode is useful for topographic

missions with the purpose to produce digital elevation models, whereas the along-track mode can be used to study movements of the ocean surface. Repeat-pass InSAR is the alternative to single-pass InSAR, and is applied in paper E. With repeated passes, a temporal aspect emerges that will affect the measured phase difference in various ways. The separation in time between the acquisitions is referred to as the temporal baseline, whereas the spatial baseline is the geometrical separation of the antenna positions.

The InSAR image (also known as interferogram) is formed by coregistering the SAR images and computing the phase difference pixel by pixel. The interferometric phase difference between the two images can be expressed as [36]

$$\Delta\varphi = \frac{4\pi}{\lambda}\Delta\eta + \frac{4\pi}{\lambda}\frac{hB_{\perp}}{R\sin\vartheta} + \frac{4\pi}{\lambda}B_{/\!/} + \Delta\varphi_{atm} + \Delta\varphi_{dielectric} + \Delta\varphi_{pn} + 2\pi n, \tag{1.9}$$

where the geometrical parameters are defined according to Fig. 1.4. $\Delta\eta$ is thus the (small) movement of the ground surface along the radar line-of-sight, h is the local surface height with respect to some reference surface, R is the slant range, $B_{\perp}$ and $B_{/\!/}$ are the normal and parallel baseline components, and ϑ is the local incidence angle. Further on, there are three parameters expressing phase differences from various effects: $\Delta\varphi_{atm}$ is the phase difference due to atmospheric effects, $\Delta\varphi_{dielectric}$ accounts for changes in the dielectric properties of the scatterers and $\Delta\varphi_{pn}$ represents phase noise.

The first term in the right-hand side of Eq. (1.9) equals zero for a stationary surface. If sea ice is present in the scene, there could for instance be a slight drift, a change in absolute sea level or sea level tilt that creates movement of the scatterers in the radar line-of-sight direction [37].

The second term specifies the influence of the normal baseline on the measured phase difference. The local topography h manifests in this term, and is amplified by the length of the normal baseline. The longer the baseline, the larger is the stereographic effect. For the purpose of mapping surface deformation with repeat-pass SAR, it is therefore essential to keep the normal baseline short in order to minimize the effect from topography. On the other hand, if the objective is to create a digital elevation model, this term is the key observable.

The parallel baseline, appearing in the third term of Eq. (1.9), arises from the separation in orbital position of the first and second fly-over. With precise orbit determination, the satellite orbits can be determined and compensated for. Sometimes the baseline can be determined to a better accuracy by estimating the registration offset between the two SAR images and use that result to estimate the baseline. The registration offset is determined in range and azimuth from the single-look complex data using for instance the coherence optimization algorithm or intensity cross-correlation optimization method [38, 39, 40].

As mentioned, $\Delta\varphi_{atm}$ is due to atmospheric effects. This parameter accounts for phase difference caused by changes in the water vapour content and distribution in the troposphere

between the two acquisitions. Rain or snow fall will have an impact on the interferometric phase difference. Also fluctuations in the ionospheric delays are included in this parameter. The atmospheric phase component is difficult to calculate, but should be corrected for [41].

$\Delta\varphi_{dielectric}$ is the phase difference caused by changes in the dielectric properties of the ground pixel. The dielectric properties of sea ice will be described in more detail in the next chapter. Changes in these properties could occur for instance through brine leakage during sea ice growth, or by structural changes in ice that is melting and disintegrating. A temperature change in the ice interior would also change its dielectric properties. These effects are often negligible on shorter time scales. Additionally, if there is a snow layer on the ice surface, the snow may be subject to changes (e.g. melting and refreezing) that alter the dielectric properties of the scattering volume.

The phase noise, expressed by $\Delta\varphi_{pn}$ in Eq. (1.9) is due to thermal noise in the receiver, quantization noise from the analog-to-digital converters, spatial and temporal decorrelation, etc. With phase noise follows a loss of coherence, which may be reduced by filtering of the interferogram, for instance by multilook processing or adaptive filtering techniques.

The last term of Eq. (1.9) wraps the interferometric phase difference into the range of observable phases, $[-\pi, \pi)$. Phase unwrapping is the process of adding an integer number of phase cycles to the measured phase in order to resolve the 2π ambiguities and retrieve a continuous phase. The unwrapped phase can be used for direct measurements of displacements. A variety of methods have been developed to perform the complex task of phase unwrapping in two-dimensional data (e.g. [42, 43]). In some applications it is however sufficient to unwrap the phase along a one-dimensional path [44].

Consider the fact that the coherent sum of contributions from the individual scatterers within a resolution cell on the ground varies with aspect angle [32]. For two images acquired from slightly different aspect angles, the effect is that the radar signals comprise different, but overlapping, ground reflectivity spectra. This can be partly compensated for by tuning the processing filters to different centre frequencies, a method known as wavenumber shift filtering [45]. The filtering method effectively compensates for the geometric decorrelation caused by the normal baseline and local terrain slope in the zero-Doppler plane. As a result of wavenumber shift filtering, a higher degree of coherence can be maintained.

The quality of the interferometric phase difference is given by the magnitude of the coherence, which is derived from the complex SAR images s_1 and s_2 at a given pixel as

$$\gamma = \frac{\mathbf{E}\{s_1 \cdot s_2^*\}}{\sqrt{\mathbf{E}\{|s_1|^2\}\mathbf{E}\{|s_2|^2\}}}, \qquad 0 \leq |\gamma| \leq 1. \tag{1.10}$$

Here, $\mathbf{E}$ denotes the expectation value. The coherence takes the form of a complex random variable [24]. The magnitude of the coherence equals one if there are no statistical errors, i.e. complete lack of random variations in pixel reflectivity, additive noise, baseline decorrelation

and temporal decorrelation.

Chapter 2

Radar backscatter from sea ice

2.1 Physical properties of sea ice

Sea ice is formed from freezing sea water. The incorporation of salt in the form of brine inclusions in the ice makes its radar signature different from freshwater ice. Sea ice is a complex mixture of pure ice in various states of crystallisation, air bubbles and brine pockets. The amount of brine in the ice increases with the rate of the sea ice growth. Brine drainage starts as soon as the sea ice is formed, but the process is rather slow during freeze-up. Both volume and surface scattering from the ice have a large effect on the radar signature. The surface roughness, defined as the root-mean-square height relative to a perfectly smooth surface, is a key parameter. Small-scale properties such as the presence of frost-flowers, pressure ridges, melt ponds, snow on the ice and hummocks are important factors with impact on the radar backscatter [46, 47, 48, 49].

Many studies have been made with the purpose to describe the varying properties of sea ice using physical quantities [15]. Basic electromagnetic quantities describe the interaction between radiation and matter. The primary parameter is the *relative permittivity*, which is a frequency-dependent quantity that characterises the electrical properties of the medium. It is denoted as $\epsilon = \epsilon' - j\epsilon''$, where the real part is a measure of energy storage within the material and the imaginary part gives the electromagnetic loss of the material. The total electromagnetic loss is a sum of absorption loss (transformation of electromagnetic energy to heat) and scattering loss. Other electromagnetic quantities can be derived from the relative permittivity, including the complex propagation constant and the penetration depth.

The constituents of sea ice — freshwater ice, liquid brine, and air — have different permittivities, and the complex permittivity of sea ice depends on two factors: 1) the volume fraction of each constituent together with 2) the geometric shape of brine pockets and air bubbles relative to the orientation of the electromagnetic wave. Pure ice consists of thin platelets that form grains with different crystallographic axes, or c-axes. For certain ice types, like frazil or mul-

tiyear ice, the crystals are arbitrarily orientated, whereas other ice types exhibit regularity in the orientation of the c-axis, as for example columnar ice. These differences affect the dielectric properties of the ice, and make them dependent also on ice type. Most of the properties will change with temperature, which makes it even more complicated to characterise the sea ice. A change in temperature is accompanied by a change in brine salinity and size of brine pockets, keeping the ice in phase equilibrium. If for example the temperature falls, the walls of the brine pockets freeze and less brine must fit into a smaller space, resulting in a rise in salinity of the remaining brine. As the newly formed ice occupies more volume than the brine, the pressure increases which causes some brine to expel through cracks around the pockets.

A snow layer on top of the ice can significantly change the radar signature of the surface. A distinction is usually made between wet and dry snow, as there is a clear difference in their electromagnetic properties. For a dry snow cover, the snow consists of ice crystals and air voids. A few snow properties affect the complex permittivity of dry snow; specifically the temperature, snow density, and shape of ice-particles. Wet snow is made up of ice crystals, liquid water, and air, where the liquid water may be saline. It has been found to exist in either of two regimes. In the *pendular* regime, air fills the pore space within the snow and liquid water is constrained to isolated inclusions. The *funicular* regime, on the contrary, is characterised by higher degree of liquid saturation. The liquid water fills the pore space within the snow, whereas air appears in the form of isolated bubbles. The relative permittivity of wet snow is determined by temperature, volumetric water content, snow density, ice-particle shape and shape of the water inclusions.

The boundary between the snow and the ice layers may be sharp, or it could be a gradual transition. Flooding may occur and fill the boundary layer with saline water, or brine may be drawn up by capillary action, producing slush at the ice-snow interface.

2.2 Surface and volume scattering

Scattering in sea ice is properly described by statistical moments of scattered fields. It is then useful to discuss the radar backscattering in terms of surface and volume scattering (see Fig. 2.1). Starting with volume scattering, one may treat the incoming beam as a coherent mean wave that is refracted and propagates into the snow/ice volume. The coherent mean wave is made up of the part of the radiation that has a constant phase relationship to the illuminating waveform. This wave will experience an effective permittivity in the medium that usually is complex. Thus the wave will be subject to scattering loss and absorption loss. The scattered waves are spread in many directions and have no consistent phase relationship relative to the illuminating waveform. This field is known as the incoherent scattered field and relates to the backscatter measured by the radar. Depending on the medium, the incoherent scattered

field may be dominated by single scattering or multiple scattering. Single scattering tends to dominate if the medium is lossy and the scattered radiation is quickly absorbed [15]. If there is multiple scattering, it means that a major part of the incoherent scattered field is scattered many times. Multiple scattering occurs if the absorption is small or if individual scatterers deflect a significant amount of the radiation. Volume scattering may be strong even if the volume fraction of scatterers is small; it depends a lot on the amount of absorption in the medium and the strength of individual scattering events.

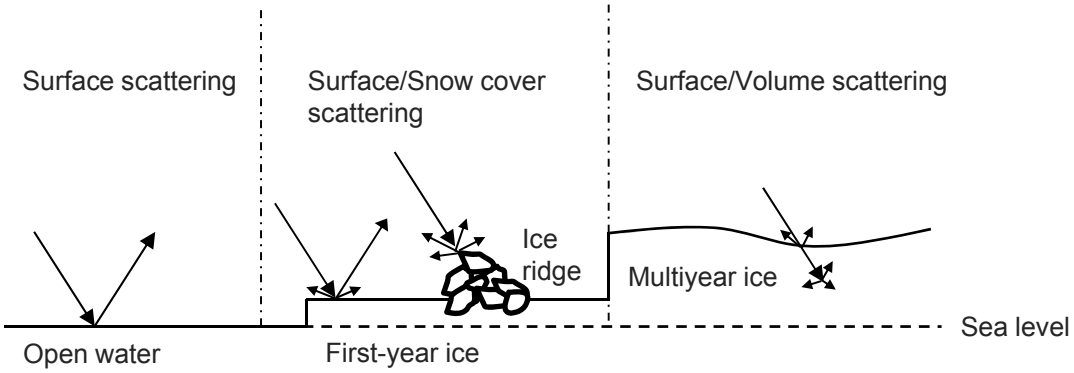

Figure 2.1: Scattering processes in open water, first-year ice and multi-year ice. From [15].

Surface scattering occurs when the transmitted beam impinges on a non-planar surface. The radiation is then scattered in accordance with Maxwell's equation. Coherent fields are reflected and refracted, whereas incoherent fields spread in all directions. Incoherent scattering dominates for a surface with a roughness comparable to the radiation wavelength. The coherent radiation thus weakens in favour of the incoherent radiation. The transition from a smooth to a rough surface occurs gradually with decreasing wavelength. According to the Rayleigh criterion, a surface is smooth if the surface roughness s fulfills

$$s < \frac{\lambda}{8\cos\theta}\,, \tag{2.1}$$

where θ is the angle of incidence. As an example, consider a C-band SAR operating at 5 GHz and a ground surface that is illuminated at an incidence angle of 40°. The Rayleigh criterion is then fulfilled if $s < 10\,\text{mm}$.

The radar return from sea ice is thus composed by a surface scattering component and a volume scattering component. This is the starting-point in many radar backscatter models [22, 50, 51, 52, 48]. Surface scattering is considered to occur in the air-snow, snow-ice, and ice-water interfaces, and volume scattering in the ice and the snow layer.

2.3 SAR polarimetry and sea ice

The first fully polarimetric SAR data over sea ice were acquired in the winter 1988 using a multi-frequency airborne SAR system [53]. The data set brought new possibilities to extract geophysically important ice variables from SAR data and motivated further campaigns. SAR polarimetry was taken to space by the Spaceborne Imaging Radar-C (SIR-C) missions in 1994 [54]. The SIR-C instrument flew on the Space Shuttle Endeavour and gathered fully polarimetric data at L- and C-bands. It was however not until the launch of ALOS and RADARSAT-2 in 2006 and 2007 (see section 3.1), that fully polarimetric SAR images became available from satellite.

Polarimetric studies of sea ice have mostly focussed on ice type classification. Early studies used various combinations of co-polar (HH and VV) and cross-polar (HV and VH) values and ratios to distinguish between ice types [55]. Several other parameters have been tested, and are still being investigated. Examples include co-polar and cross-polar phase differences, and phase and magnitude of the complex correlation between backscatter channels [53, 56]. A general survey of these methods pointed out, however, that multi-frequency SAR data is more effective than fully polarimetric single-frequency data for ice classification [57].

Other applications of polarimetry include thin ice detection and estimation of ice thickness [53, 58, 59, 60]. It has been seen that the ice thickness is linked to the VV-to-HH backscattering ratio with C-band data as well as L- and X-bands. The linkage is explained by the relation between the backscatter ratio and the near-surface dielectric constant, which in turn is an indicator of the developed ice stage and thereby also the ice thickness. The co-polar phase difference has also been studied and shown to be related to variations in thin ice thickness at C- and L-band [61, 62].

The more recent developments in the field of radar polarimetry build mostly upon target decomposition theorems [63]. A number of different decompositions have been proposed since the original work. These decomposition techniques can be divided into four types [64]: 1) Those based on the dichotomy of the Kennaugh matrix, 2) Those based on a model-based decomposition of the covariance matrix or the coherency matrix. 3) Those using an eigenvector or eigenvalues analysis of the covariance matrix or the coherency matrix. 4) Those employing coherent decomposition of the scattering matrix. An example of this type of decomposition is the Pauli decomposition, which is illustrated in Fig. 2.2. The Pauli decomposition can in the monostatic case be interpreted as a composition of three scattering mechanisms: the first being single scattering from a plane surface (single or odd-bounce scattering), the second and third being diplane scattering (double or even-bounce scattering) from corners with a relative orientation of 0° and 45°, respectively.

For the purpose of ice classification, decompositions from group (2) and (3) have been used in [65], from group (3) in [66], and groups (2)-(4) in [67]. These publications are just a few

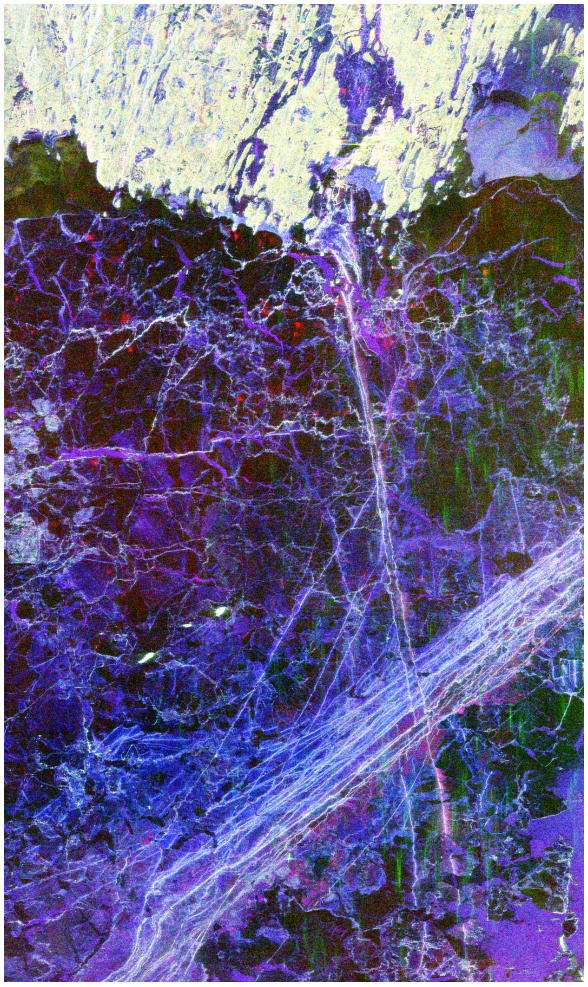

Figure 2.2: Pauli decomposition (i.e. coherent decomposition of the scattering matrix) of an ALOS PALSAR scene from March 27, 2009, in the Gulf of Bothnia. The scene covers an area of 30 by 50 km with the city of Umeå, Sweden, located at the upper edge.

examples showing the work being made towards automatic segmentation of fully polarimetric SAR images.

Chapter 3

Material and methods

This chapter provides an overview of the material and methods that have been used in the thesis. First a description of the SAR data relevant to the thesis is provided. The following part gives an overview of the different types of measurements that have been carried out during field campaigns. The purpose of these campaigns were to provide reference data (ground truth) for validation of algorithms that use SAR data for making estimates of sea ice parameters, and for analyses of the acquired SAR imagery.

3.1 SAR data

Table 3.1: SAR platforms and sensors used in this thesis.

Platform	Lifetime	LTAN	Sensor	Freq. [GHz]	Polarisation
Envisat	2002 – 2012	10:00 am	ASAR	5.331 (C)	Single/Dual
ALOS	2006 – 2011	10:30 am	PALSAR	1.270 (L)	Single/Dual/Quad
TerraSAR-X	2007–	6:00 pm	TSX-SAR	9.650 (X)	Single/Dual/Quad*
COSMO-SkyMed	2007–	6:00 am	SAR-2000	9.600 (X)	Single/Dual
RADARSAT-2	2007–	6:00 am	SAR	5.405 (C)	Single/Dual/Quad

*Quad-Pol only in experimental mode

An increasing number of SAR satellites were launched in the early 2000's, providing better coverage in space and time and more choices of frequency, polarisation, and different imaging modes. In this thesis, five SAR satellites were used, and these are listed in Table 3.1. The satellites fly in sun-synchronous orbits at altitudes ranging from 500 km to 800 km and with an orbital period of about 100 minutes. These orbits provide near-global coverage, but leave a circular data gap around the poles. The maximum latitude of the orbits ranges from 81.4° N for RADARSAT-2 to 82.6° N for TerraSAR-X. The orbits are usually defined by the local time

of the ascending node (LTAN) as the satellite passes the equator [68]. Having LTAN close to dusk or dawn is beneficial for active microwave satellites as the solar panels will be exposed to sunlight during the entire orbit.

The ScanSAR mode is normally preferred for operational sea ice mapping as it generally gives the best combination of swath width and resolution for synoptic ice monitoring [69, 70]. The properties of the ScanSAR mode vary between different radars. Table 3.2 provides a comparison for the ScanSAR modes of the satellites considered in the thesis.

Table 3.2: Comparison of ScanSAR modes for selected SAR sensors.

SAR Platform	Mode	Swath width [km]	Pulse bandwidth [MHz]	Spatial res. (rg × az) [m]	Polarisation
Envisat	Wide Swath (WS)	400	15	150×150 at 7×3 lks	HH or VV
ALOS	Wide Beam (WB)	350	14	$71\text{–}157 \times 100$ at 4×2 lks	HH or VV
TerraSAR-X	ScanSAR (SC)*	100	100–150	$17\text{–}19 \times 19$ at $5\text{–}11 \times 1$ lks	HH or VV
COSMO-SkyMed	ScanSAR Huge (HR)	200	9–24	100×100 at 5×3 lks	HH, HV, VH or VV
RADARSAT-2	ScanSAR Wide (SCW)	500	12	$72\text{–}160 \times 100$ at 4×2 lks	HH, HV, VH, VV, HH+HV or VV+VH

*A new wide-angle mode was introduced in 2013, offering a swath between 200 km and 270 km with a resolution of 40 m × 40 m.

3.1.1 Envisat

The ESA (European Space Agency) satellite Envisat was launched in 2002 and carried the ASAR (Advanced SAR) C-band radar sensor. Equipped with totally nine instruments for Earth observation and with a weight of more than eight tonnes, it was the largest civilian Earth observation satellite ever put into space [71].

The ASAR sensor offered imaging in five different modes, of which two will be considered in the thesis. For regular sea ice monitoring and ice charting, the wide swath mode has been essential. In this mode, the images are co-polarised in either HH- or VV-polarisation. The swath was divided into five smaller sub-swaths (extending in the along-track direction), which the antenna scanned in elevation. The image shown in Fig. 3.1 was acquired in this mode.

In the alternating polarisation mode, the radar acquired two images in different polarisations. Three setups were available, either two co-polarised images (HH+VV) or one co-polarised and one cross-polarised (HH+HV or VV+VH). Images acquired in this mode have a spatial

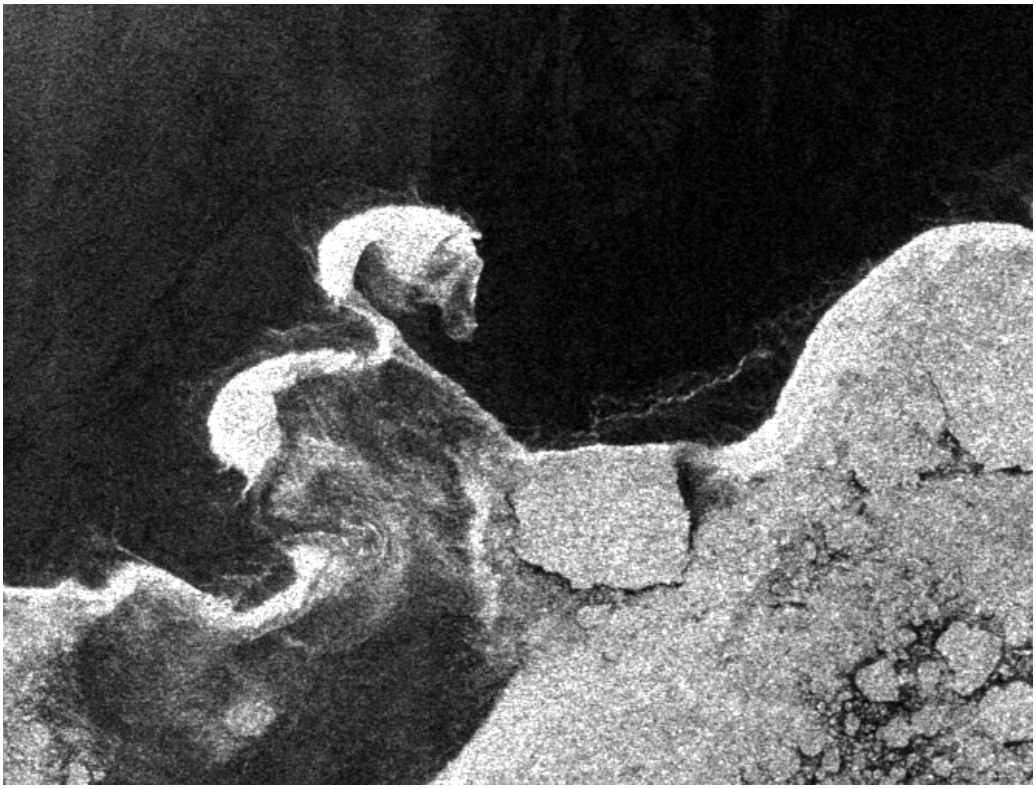

Figure 3.1: Section of an Envisat ASAR wide swath scene in HH polarisation from August 20, 2011. The image shows the ice edge north of Svalbard from a descending orbit and covers an area of 50 km × 40 km.

resolution of approximately 30 m with a swath width between 56 km and 100 km. The Envisat mission was ended after communication with the satellite was lost on April 8, 2012.

3.1.2 ALOS

ALOS (Advanced Land Observing Satellite) was launched by JAXA (Japan Aerospace Exploration Agency) in 2006. It was equipped with the L-band PALSAR (Phased Array type L-band SAR) sensor. As the name of the satellite suggests, the primary purpose of the mission was dedicated to land observation. The Baltic Sea was however covered in some phases of the observation plan, and images could be obtained in three out of five modes: in fine beam mode, polarimetric mode and ScanSAR mode. The fine beam mode gives finest spatial resolution, around 5 m and with a swath width of 70 km. Polarimetric mode offered fully polarimetric images with slightly coarser resolution and a swath width of 30 km. The third mode is the ScanSAR mode which operates with five sub-beams by default. ALOS was decommissioned on May 12, 2011.

3.1.3 TerraSAR-X

The German TerraSAR-X satellite mission was implemented in a public-private partnership between the German space agency DLR (Deutsches Zentrum für Luft- und Raumfahrt) and EADS Astrium. The satellite carries an X-band SAR and operates in stripmap, spotlight or ScanSAR mode. Besides ScanSAR images, images in stripmap mode have been acquired and studied within the scope of the thesis. Stripmap mode provides images in single polarisation with a swath width of 30 km and a resolution of 3.5 m.

3.1.4 COSMO-SkyMed

The Italian COSMO-SkyMed satellite constellation consists of four identical, mid-size satellites equipped with X-band SAR. The satellites follow the same ground track which repeats after 16 days, and the same spot is revisited within time intervals from 1 to 15 days. The constellation is thus able to carry out interferometric acquisitions with a variety of temporal baselines. The satellites deliver products in ScanSAR, stripmap and spotlight mode. There are two stripmap modes, Himage and PingPong, of which the former has single polarisation and the latter has dual polarisation.

The COSMO-SkyMed mission is, at present, the only SAR constellation which is dedicated to both civilian and defence use [72].

3.1.5 RADARSAT-2

RADARSAT-2 is a Canadian C-band SAR satellite and a follow-on mission to RADARSAT-1 [73]. The most significant upgrade of RADARSAT-2 was the introduction of an active phased array antenna which enabled two-dimensional beamforming and beamsteering. The satellite has ability to operate in seventeen different beam modes, including spotlight, stripmap, ScanSAR and fully polarimetric modes. RADARSAT-1 proved the value of SAR data for ice charting, and RADARSAT-2 was designed to assure continuity of the supply of radar data for ice services as well as other end users. The new option to acquire dual polarisation data in ScanSAR mode is specifically valuable for operational ice charting [70].

3.2 Field measurements

The quality of the SAR derived ice drift and concentration estimates needs to be assessed with field measurements. These measurements are normally referred to as “ground truth”, despite the fact that also field observations are subject to uncertainties. Knowledge of the ground truth aids data interpretation and analysis and may also be used for calibration purposes. This

section will examine three types of field measurements of relevance to the thesis: airborne imagery, ice buoy measurements, and manual measurements performed directly on the ice.

Airborne measurements were carried out in order to support the analysis of ice concentration products as well as for ice type classification in paper D. These type of measurements are beneficial as large areas can be covered in a short time and one can easily move to places of interest. The analyses can sometimes be difficult even for aerial photos, as for example dark nilas may be difficult to distinguish from open water and white foam may be taken for slush ice.

The flights were conducted in the northern Baltic Sea, by helicopter departing from Umeå Airport. On-board the helicopter was mounted two nadir-looking cameras: one infrared and one optical camera. The flight altitude was nominally 2000 ft, resulting in a swath width for the optical camera of about 1.5 km. The infrared sensor has a smaller angle of view and covers about a sixth of the same width. The acquired photos were geotagged by the use of GPS receivers. The basic flight strategy was to fly in parallel lines to cover a specific area or to follow the ice edge in order to determine the ice extent.

Ice buoys are an important resource for gathering in-situ information during long time periods. An ice buoy is deployed on a drifting ice floe and transported along with the floe. The buoy can be equipped with multiple sensors that record environmental data such as temperature and air pressure. Measurements of the position are essential and can later be compared to SAR measurements of the ice drift [74].

During the Baltic field campaigns, an ice buoy was deployed in the central Bay of Bothnia. The buoy was equipped with rotary encoders that would record the three-dimensional attitude of the buoy. The purpose of measuring the attitude is to learn at which time the ice has melted and the buoy starts to float in open water. Also the temperature on the bottom side of the buoy was measured and evaluated for the same purpose. Two other thermometers measured the temperature inside and on top of the buoy.

The last type of field measurement of relevance to the thesis is manual measurements carried out on the ice. These were made to aid the interpretation of the SAR images in paper D. Drill holes were made to measure the thickness of the ice and snow layers. The snow density was determined, and the upper part of the ice core was inspected for air bubble quantification.

3.3 Ancillary data

Ancillary data have been gathered from external sources in those cases where data have been accessible and applicable. Paper A uses ice charts produced by the Swedish Ice Service at the Swedish Meteorological and Hydrological Institute (SMHI) as reference data for sea ice concentration. The ice charts are produced daily during the ice season, and cover the Baltic Sea,

Skagerrak and Kattegat. The charts are drawn by ice analysts using the most recent available satellite data, often from SAR images, but from optical imagery as well. Ship observations from icebreakers and other vessels are used as an additional information source. The analysis of the ice conditions relies on the ice chart produced from the previous day, which contributes to a high level of reliability that cannot be achieved from classification of a single SAR image.

In paper E, meteorological and hydrological stations are used to gather information about weather conditions and sea level. SMHI is operating around 20 measurements stations that provide measurements of sea level along the coast of Sweden. The system used is a stilling well gauge, which is able to suppress fast water level variations from waves [75]. The water level is measured in number of centimeters above the annual average sea level.

Weather data were obtained from measurements at the Kemi-Tornio airport in paper E. These were ordinary data describing the weather conditions. The studied parameters include air temperature, wind speed and direction, cloudiness and precipitation. The presented wind speed and direction is the average over an interval of 10 minutes, and the precipitation is accumulated over periods of one hour.

Chapter 4

Retrieval of ice parameters

4.1 Sea ice concentration

Sea ice concentration is an important variable in climatology as well as for ice charting. It is defined as the areal fraction of the ocean surface that is covered with ice within a given region. The ice concentration has been measured globally on daily basis since 1979, using passive microwave radiometers flown on the Nimbus program and DMSP (Defense Meteorological Satellite Program) series of satellites [16, 76]. There are three generations of these radiometers, as listed in Table 4.1.

Table 4.1: Passive microwave sensors in the Nimbus and DMSP programs.

Sensor	Abbr.	Operational	#Frequencies/#Channels
Scanning Multichannel Microwave Radiometer	SMMR	1978 – 1987	5/10
Special Sensor Microwave / Imager	SSM/I	1987 –	4/7
Special Sensor Microwave Imager / Sounder	SSMIS	2005 –	21/24

The sea ice concentration (or sea ice extent, a binary classification into sea ice and open water, usually divided at 15% ice concentration — see e.g. [77]) can also be determined from SAR imagery [78], with higher spatial resolution but lower spatial and temporal coverage. If there is daylight and no clouds obscuring the view, optical satellite images may also be used to determine the ice extent.

Early studies dealing with discrimination of open water and sea ice in SAR images utilised statistical and textural properties of the images. One of the first approaches based on statistical properties is presented in [79]. The local brightness and variance span a two-dimensional feature space which is divided into two classes by a first-order polynomial. A study made in the Baltic Sea revealed that the method in general is uncertain [80]. Other approaches based on thresholding local brightness were presented in [81], [82], and [83]. The last was developed for

Arctic summer conditions and added passive microwave data from SSM/I to classify regions of open water, where wind-roughened areas otherwise may be interpreted as ice.

The use of various texture-based methods for estimating the sea ice concentration has been studied thoroughly. Gray Level Cooccurrence Matrices (GLCM) has shown to perform well compared to other texture feature extraction methods [84], but does not rule out the value of standard statistics [85]. GLCM can be used e.g. with a Bayes classifier to separate ice and water with high accuracy [86, 87]. Block-wise mean auto-correlation has proved to give typically very low values over open water, and thus to be a useful tool for classification of open water and sea ice [88]. In [89], a segmentation-based algorithm is described which utilises the auto-correlation. Segmentation is performed with a pulse-coupled neural network and is further refined after the autocorrelation has been computed. If a segment has a mean autocorrelation below a certain threshold, it will be classified as open water. The open water segment will be extended to neighbouring segments if they meet a slightly looser condition. Comparison with operational sea ice charts showed the algorithm located open water with an accuracy of about 90 percent. A developed version of the algorithm was presented in [90], in which a new module was introduced to identify fast ice, and also in [91], where the incorporation of cross-polarised data is shown to improve the ice concentration estimation. Polarimetric L-band data were used to determine the ice concentration in [92]. The division between sea ice and open water was based on the scattering entropy, which is lower over open water where only one type of scattering mechanism, surface scattering, dominates. In scattering from sea ice, there are multiple scattering mechanisms involved, which results in higher scattering entropy.

The ice concentration algorithm presented in paper A is based on the auto-correlation approach. It combines the weighted mean auto-correlation with local brightness of single-polarised SAR images using a neural network. The algorithm determines internally local sea ice and open water intensities based on the measured auto-correlation.

4.2 Sea ice drift

Sea ice drift is the speed and direction at which the sea ice moves relative to the Earth. Sea ice drift can be measured with buoys that are anchored on drifting ice. The buoys determine their positions with for instance GPS receivers and store the information internally. The position data can then be transmitted via satellite link or recovered along with the buoy. Underwater sensors are also used to measure sea ice drift, specifically upward-looking Acoustic Doppler Current Profilers (ADCP) [93, 94]. ADCPs may be deployed on bottom-anchored subsurface moorings and are usually accompanied by Upward Looking Sonars (ULS). An ADCP transmits acoustic energy along four beams at an angle off the vertical, in the form of an upside down cone. The Doppler effect gives the velocity of the scatterer along the direction of each beam. In

comparison, a ULS makes high frequency measurements of sea ice draft using a single, narrow beam, and are not used for direct measurements of ice drift. A third method to measure sea ice drift is from consecutive satellite images. Passive microwave data can be used as well as SAR images for the purpose of tracking sea ice [95, 96, 97, 98]. Here SAR outperforms passive microwave when it comes to detail and accuracy of the measurements. On the other hand, the regularity of the measurements and the daily, global coverage are advantages of the passive microwave sensors [82].

The first SAR measurements of sea ice motion was presented in 1979 and used airborne L-band SAR data from the Arctic Ice Dynamics Joint Experiment [99]. The ice drift was measured with a feature tracking approach. Homologous ice features were visually identified in sequential radar images, and the drift was estimated by comparing the corresponding map coordinates. The same approach was used to measure ice motion in L-band SAR data acquired by NASAs Seasat satellite in 1978 [100]. The cross-correlation technique was employed a few years later for ice motion estimates with Seasat images [101]. The hierarchical (or pyramidical) multi-resolution approach was introduced at the same time. A crude displacement field is attained with highly averaged images, whereupon the resolution is increased successively in order to refine the motion field. The multi-resolution approach was adopted in [102], which also evaluated different types of median filtering of the motion field. The algorithm presented in [102] was employed in [103], which pointed out the difficulty in tracking ice in the inner marginal ice zone.

The cross-correlation method has later been supplemented with the phase correlation method [104] and the optical flow method [105]. The phase correlation method was first used for sea ice drift in a study to estimate pack ice motion with Advanced Very High Resolution Radiometer (AVHRR) imagery [106]. Later on, the method was used to measure also glacier velocity [107]. Feature-based tracking was combined with phase correlation in an ice-motion tracking system developed for the Alaska SAR Facility [95].

A comprehensive ice motion algorithm based on both phase correlation and normalized cross-correlation has been suggested by M. Thomas [108]. The phase correlation is evaluated at different image resolutions using an hierarchical processing pyramid. The same approach was used to develop the sea ice drift algorithm which is presented in paper C.

The same algorithm was used to compile Fig. 4.1 and 4.2, showing the ice drift in the Fram Strait over a one-year period. Starting in spring in April 2011, four seasons are covered until the end of March 2012. A total of 352 images were combined into 684 combinations of image pairs. The drift was averaged for periods of two months length. Unfortunately, there is a lack of data for the autumn and early winter of 2011 due to a problem with the automatic data selection and transferring. Nevertheless, there are still enough data to reveal the seasonal trends. The correlation has been used as a quality measure, and pixels with low correlation were ignored

while means were computed. (In the figures, the correlation is scaled such that the maximum observed value corresponds to white colour.) This approach will mask out areas of open water. There is a downside, though, in that correct drift measurements with low correlation will be masked out as well.

A more sophisticated quality measure would possibly be able to resolve this issue, and such a quality measure has in fact been suggested by Hollands [109]. The proposed *confidence factor* still takes the correlation into account, but considers a few other factors as well. The textural pattern is one of them, and three different texture measures are used. It also handles localized intensity peaks, originating from mirror reflections in the ice. Last in the list of quality indicators is a method known as back-matching. Back-matching means that the two SAR images are processed in the reverse order, resulting in the drift being estimated from the image acquired last to the first image. If, at a certain position, the "reverse" drift vector is added to the "forward" drift vector, the original position should be obtained for error-free measurements. Thus, the magnitude of this vector sum forms input to the confidence factor. One shall note that the basis for back-matching lies in the subimage alignment at the topmost processing level. If the subimages are aligned in the same way in both the forward run and the reverse run, the motion fields would correspond exactly to each other; simply because the algorithm is deterministic. Thus, effectively the same result could be achieved if ordinary forward-matching is performed twice with a small change in the alignment of the subimages during the second run.

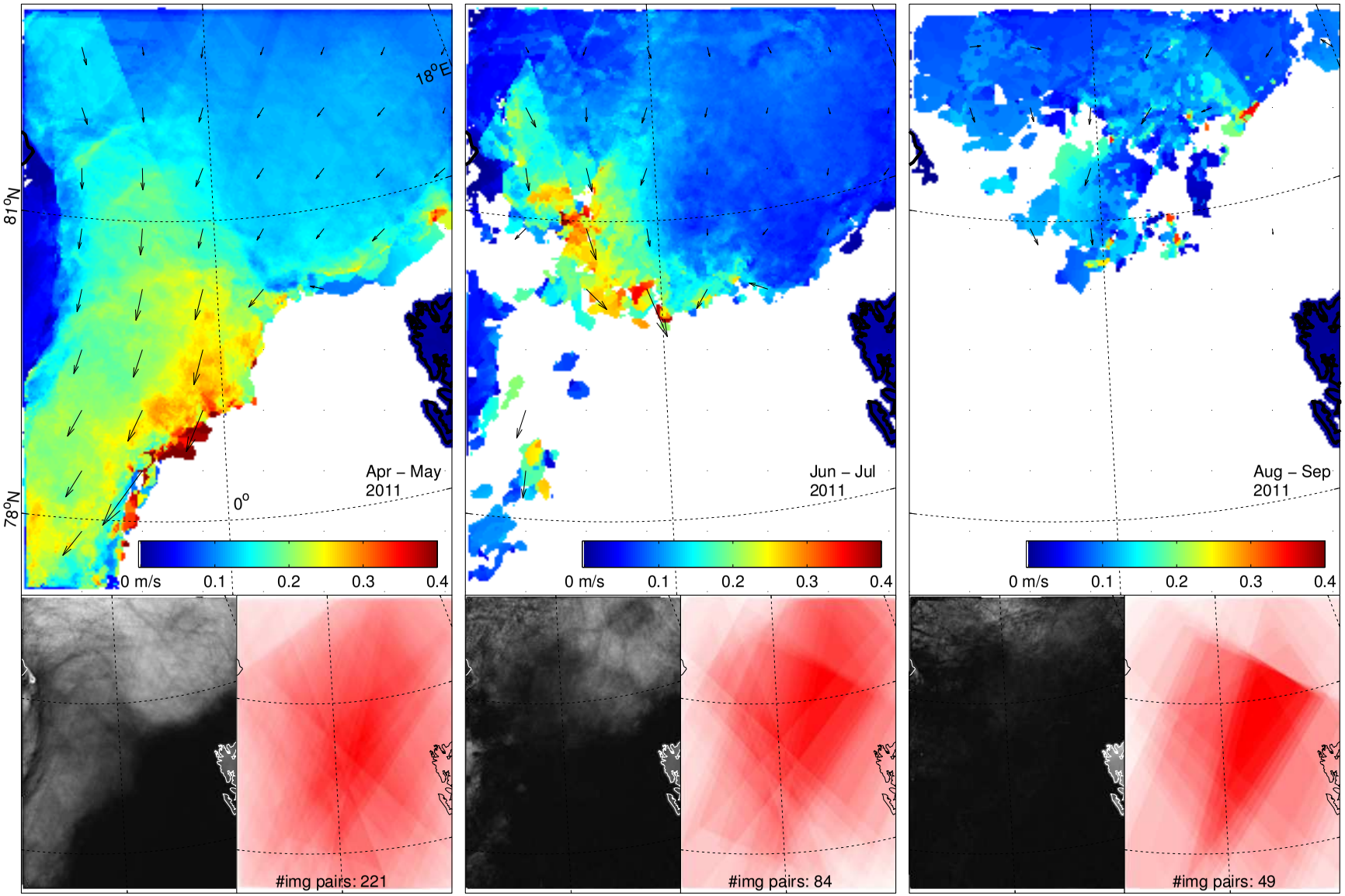

Figure 4.1: Six months of ice drift in the Fram Strait, starting in April 2011. Upper plots: Mean ice drift in m/s. (White areas are open water or poorly traced ice.) Gray-scale images: Mean cross-correlation. Red images: Spatial distribution of data.

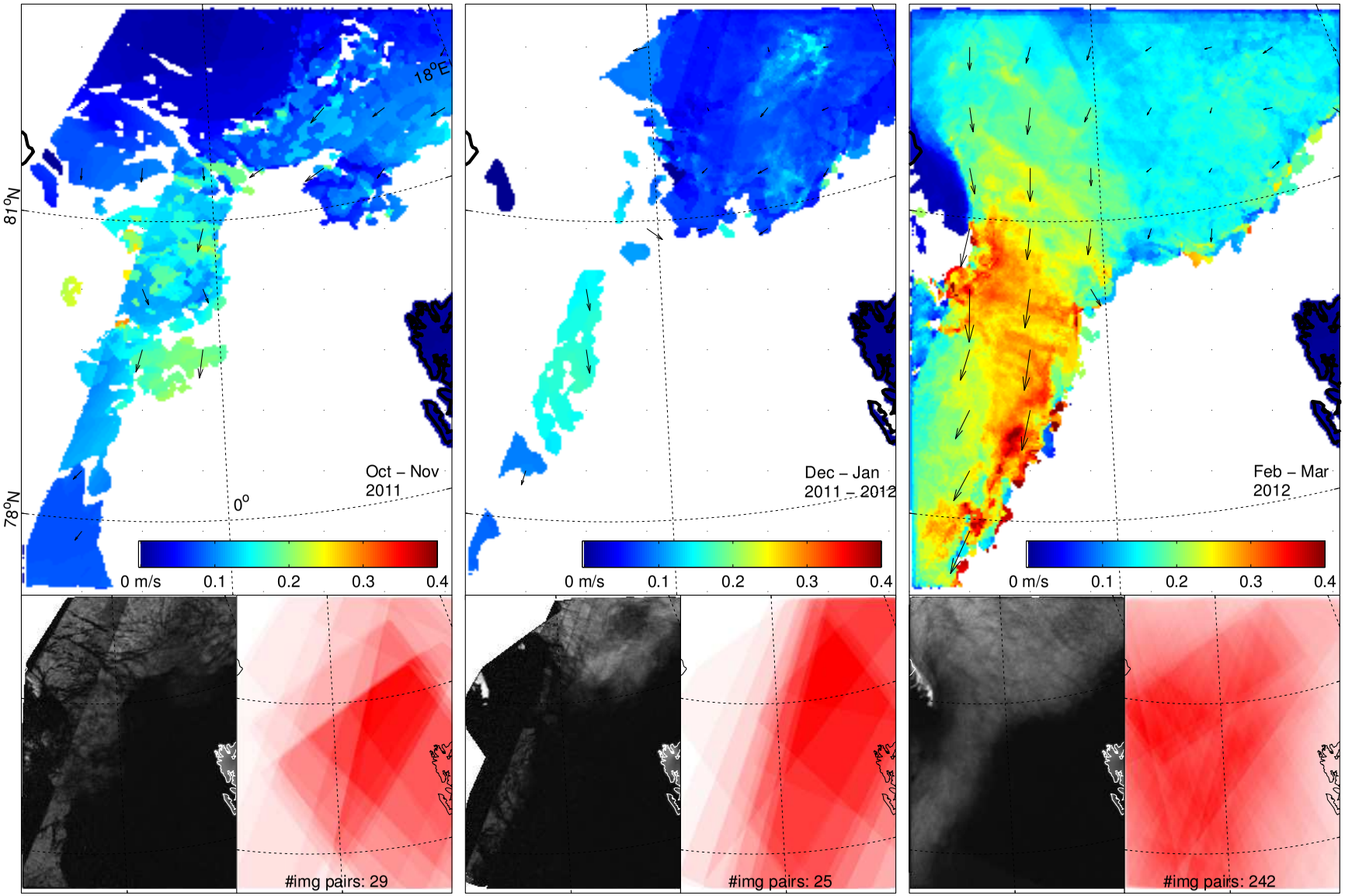

Figure 4.2: Six months of ice drift in the Fram Strait, starting in Oct 2011. Upper plots: Mean ice drift in m/s. (White areas are open water or poorly traced ice.) Gray-scale images: Mean cross-correlation. Red images: Spatial distribution of data.

Chapter 5

Sea ice modelling

5.1 Basic model elements

Dynamic-thermodynamic sea ice models have a variety of applications [110]. Short-term models are used to forecast ice conditions. The forecasts are needed for shipping and marine operations as well as a part of weather forecasting. The location of the ice edge is one example of the parameters with large implications on the short-term weather predictions. There are also specific models used to model the drift and dispersion of oil spills in ice-infested waters. These models need to take into account ice bottom roughness, dynamic state of the ice, fine scale porosity of the ice and floe size distribution. Opposite to short-term models, climate models are used to study the dynamics of the climate system and to make projections of future climate. The sea ice is modelled as a part of a coupled ice-ocean or atmosphere-ice-ocean model, and affects the fluxes of momentum, heat and matter between the air and the sea.

Sea ice modelling involves giving a thermodynamic description of the ice growth and melt, as well as equations for the ice dynamics. The latter may be derived from momentum balance and conservation of mass (e.g. in terms of ice area and volume). Further components of an ice dynamics model are descriptions of the sea ice state and sea ice rheology. The sea ice state can for instance be defined as an ice thickness distribution, as the ice thickness of one or many ice types or as ice thickness and concentration. The choice of description is made by the modeler and will, together with the choice of ice rheology, to a large extent characterize the model.

The component of the sea ice model that deals with ice rheology defines how the ice stress is affected by strain and strain rate in the ice. The ice stress depends also on the state of the ice, which then forms an additional input to the ice rheology. Modelling the ice rheology involves the selection of a rheology model, which for instance can be a viscous plastic model or an elastic-plastic model.

Once we have a full description of the model, there are three unknowns for which the equations normally are solved [111]:

- the ice velocity, which is obtained from the momentum equation
- the net ice growth or melt, which is obtained from a thermodynamic equation
- the ice state, obtained by solving the conservation equations that include thermodynamical growth and mechanical deformation (thickness redistribution)

The momentum balance (or conservation of momentum) and conservation of mass are two fundamental laws in sea ice modelling. We will now look deeper into these basic principles and how they are formulated.

5.1.1 Momentum balance

Newton's laws of motion imply that the total momentum in a closed system is constant. The conservation of momentum is used to derive the momentum equation, which can be formulated as [110]

$$\rho h \frac{D\mathbf{u}}{Dt} = \nabla \cdot \boldsymbol{\sigma} + \mathbf{F_{ext}}, \tag{5.1}$$

where ρ is the ice density, h is the ice thickness, $\mathbf{u}$ is the velocity, $\boldsymbol{\sigma}$ is the internal ice stress tensor (i.e. the horizontal stress due to horizontal interactions, integrated through the ice thickness, and thus of unit force/length), and $\mathbf{F_{ext}}$ is the sum of external forces acting on the ice in terms of force per unit area.

The acceleration term on the left-hand side in Eq. (5.1) is negligible at time scales of a few hours or more. It is included if the modeler wants to resolve inertial oscillations which occur in high frequency ice motion [111].

The first term on the right-hand side of the momentum equation, the divergence of the stress tensor, is due to forces from spatial stress differences in the ice field. These forces act to smooth the velocity field, to fulfil boundary conditions, and to transmit momentum over long distances. The stress tensor is determined from the ice rheology model, which is applied precisely here. The internal stress is intricately linked to the strain, strain rate and ice state, which is why the ice rheology is handled in quite different ways by different models.

The last term accounts for external forces acting on the ice. These include atmospheric (wind) forces on the upper surface and oceanic drag forces on the ice underside. The Coriolis effect is also taken into account by this term, as well as a force from sea surface slope. The force from sea surface slope is however relatively small and can often be neglected. Fig. 5.1 illustrates the typical force situation for drifting sea ice.

One may note that Eq. (5.1) treats the ice as a two-dimensional continuum as opposed to discrete particles. The continuum model used here is considered to be applicable in meso-scale and large-scale models, whereas the discrete particle approach has been used by models

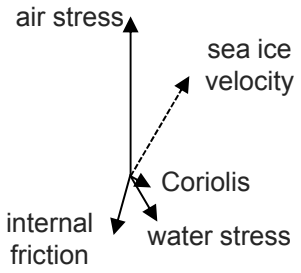

Figure 5.1: Typical picture of the major forces acting on drift ice. Valid for the Northern hemisphere. From [110].

operating on local or regional scale where individual floes or densely packed collection of floes create irregularities [112]. Efforts to develop a compromise model between the continuum and discrete particle models have also been made [113].

5.1.2 Conservation of ice mass

There are two source terms to the ice state: thermodynamical growth rate and mechanical deformation. The thermodynamic ice growth and decay are driven by heat exchange with the ocean and the atmosphere. On the ice underside, the total heat exchange is the sum of the upward heat flux from the ocean into the ice and the heat conducted away from the ice to the water. The upper ice surface is usually subject to heat loss to the atmosphere during the winter, while in summer heat flows into the ice. New ice may also form on the upper surface by submergence and flooding on the ice if there is a snow load on the ice.

The second source term to the ice state, mechanical deformation, is sometimes described as a thickness redistributor. It is affecting the ice state by advection and dynamic opening or closing. The conservation laws for ice are needed for area (in terms of ice concentration A) as well as for thickness h, and can be expressed as [114]

$$\begin{aligned} \frac{Dh}{Dt} &= -h\nabla \cdot \mathbf{u} + \Phi_h(h) \\ \frac{DA}{Dt} &= -A\nabla \cdot \mathbf{u} + \Phi_A(A), \end{aligned} \tag{5.2}$$

where $\Phi_h(h)$ and $\Phi_A(A)$ are source terms for mean ice thickness and concentration. These source terms control the thermodynamical growth and mechanical deformation. The ice concentration is constrained so that $0 \leq A \leq 1$.

One may note that the ice state is described by two separate parameters, A and h. The model is thus referred to as a two-level model. The two-level approach was introduced in the model by Hibler [115], which has become a benchmark for most of the sea ice dynamics models used today (e.g. [116, 117, 118, 119]). The model was developed further in [120] by introducing

an areal ice thickness distribution for the ice state description. Hibler's model was also used to develop a model for the Baltic Sea in [121]. This model uses two thickness parameters — undeformed and deformed ice thickness — to describe the ice state.

5.2 The HIROMB model

A very brief description of the HIROMB (High Resolution Operational Model of the Baltic Sea) model is provided in this section as an example of an ice-ocean coupled model. The model is used in appended paper C. HIROMB is a three-dimensional ocean circulation model designed for daily, operational use. Forecasts are made for currents, salinity, temperature, and ice state, among other parameters, and are short and medium-range, ranging from a few hours up to four weeks ahead [122]. The model is forced with atmospheric model data, for instance from HIRLAM (High Resolution Limited Area Model).

HIROMB was initially developed for the Baltic Sea and the North Sea. The model area was chosen to cover regions of interest and to optimize the open boundaries (e.g. to the North Atlantic) from a computational and physical point of view. The operational forecasts started in 1995. More recently, the model has been set up for the Arctic Region. An example of an ice concentration forecast by the model for the Fram Strait is shown in Fig. 5.2.

HIROMB is based on the ocean primitive equations [123], which essentially control the large scale ocean circulation. The equations consist of Navier-Stokes equations with some simplifying approximations. Based on the numerical technology of the model and the model dynamics, the model may be divided into three parts: a barotropic component, a baroclinic component, and an ice model [124].

In the barotropic part, density is a function of only pressure. Vertical integration gives the water level changes over the model surface. The baroclinic part makes use of all depth levels. The water temperature and salinity are computed in each grid point. The three-dimensional grid has fixed levels of depth in the vertical, with varying spacings, whereas the horizontal discretization is uniform.

The sea ice model has a dynamic and a thermodynamic component. These two components are used to compute forces and deformation as well as thermodynamic growth and melting. The thermodynamic model used by HIROMB is based on the Semtner zero-level model [125] and will not be detailed here. The ice dynamics model is based on the work by Hibler [115] and is highly nonlinear. The momentum balance follows the description in Eq. (5.1), but is formulated in a spherical coordinate system. Like many other ocean models, HIROMB uses spherical coordinates in the horizontal. The internal stress tensor appearing in Eq. (5.1) is a second-order tensor with four components, where two components denote normal stress (σ_{11} and σ_{22}) and the other two denote shear stress (σ_{12} and σ_{21}). The components are given by

$$
\begin{aligned}
\sigma_{11} &= \zeta(\dot{\epsilon}_{11} + \dot{\epsilon}_{22}) + \eta(\dot{\epsilon}_{11} - \dot{\epsilon}_{22}) - \tfrac{P}{2} \\
\sigma_{12} &= 2\eta\dot{\epsilon}_{12} \\
\sigma_{21} &= 2\eta\dot{\epsilon}_{21} \\
\sigma_{22} &= \zeta(\dot{\epsilon}_{22} + \dot{\epsilon}_{11}) + \eta(\dot{\epsilon}_{22} - \dot{\epsilon}_{11}) - \tfrac{P}{2},
\end{aligned}
\tag{5.3}
$$

where ζ and η are nonlinear bulk and shear viscosities, P is a reference pressure that characterizes the ice strength (an empirical function of thickness and concentration), and $\dot{\epsilon}_{ij}$ are strain rates. The strain rates are directly derived from the velocity gradient. The bulk and shear viscosities are modelled based on invariants of the strain-rate tensor, following Hibler, but with modifications to allow for stresses outside the so-called yield curve. The ice rheology in HIROMB is therefore viscous-viscoplastic as opposed to Hibler's viscous-plastic model.

The implementation of ice conservation in HIROMB's ice dynamics model follows Eq. (5.2), with $\Phi_h(h) = 0$ and $\Phi_A(A)$ being a sink term which is referred to as a ridging function. The ridging function prevents the ice concentration from exceeding 1 in case of convergence. The thermodynamic model, with advection of ice (thickness, compactness and snow cover), is simulated in the subsequent model step.

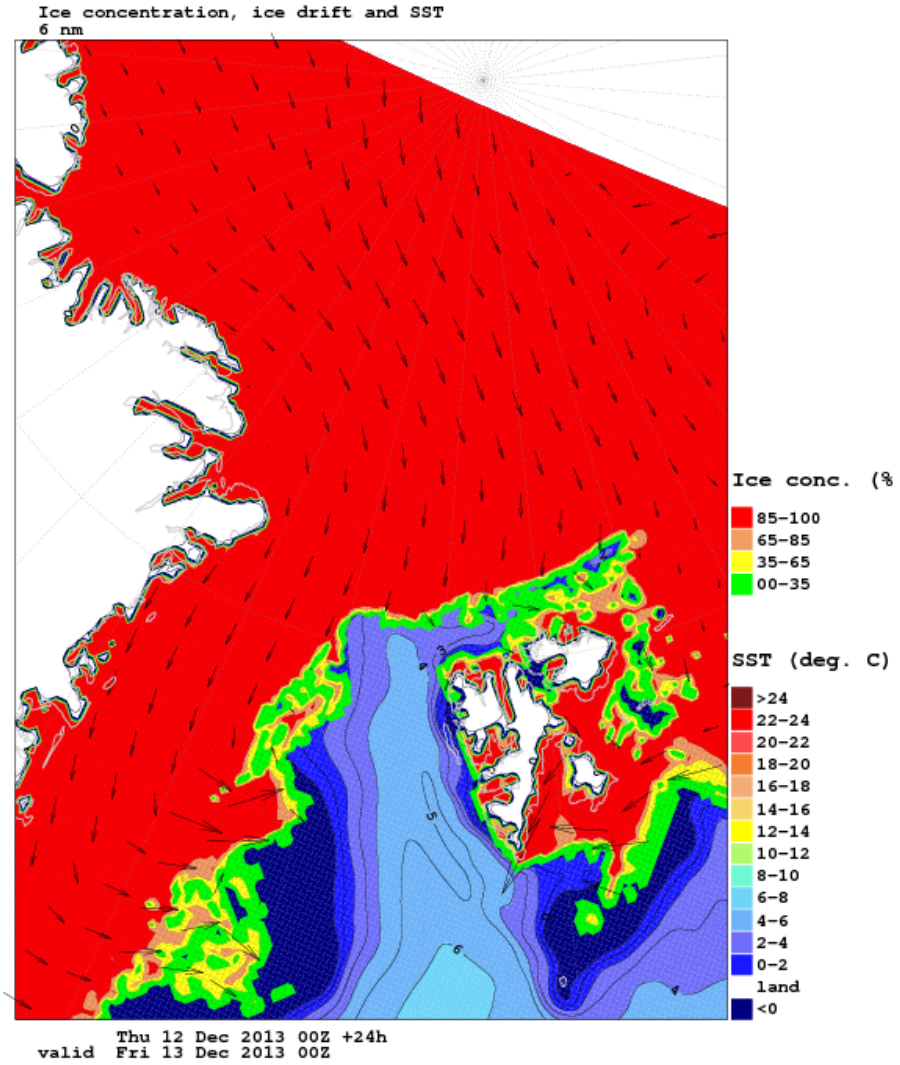

Figure 5.2: 24-hour forecast by the HIROMB model for the Fram Strait on a 6 nm grid. Colours represent ice concentration and sea surface temperature (SST), and vectors indicate the ice velocity.

Chapter 6

Summary of appended papers

This section aims to provide a short summary of the appended papers and presents the most important conclusions against the background given by previous chapters.

6.1 Paper A

In paper A, a sea ice concentration algorithm is presented. The algorithm is based on spatial autocorrelation and backscatter intensity in C-band SAR images. The two parameters, autocorrelation and intensity, are fed to a neural network that combines the inputs and map the result to values of ice concentration. The neural network is trained with ice charts from the Swedish Ice Service at the SMHI. The ice charts are produced by ice experts, whose analysis is based on visual interpretation of SAR images primarily. Additional sources of information used by the ice experts include optical imagery, ship observations, knowledge of past ice conditions, etc.

The autocorrelation over sea ice is generally higher than over open water, which is used as a basic principle by the algorithm. This condition is due to the fact that the radar signature over sea ice shows a lot of structure, e.g. from ridges, cracks, floe boundaries, changes in surface roughness, etc., whereas the open water has a more noise-like signature. While this disparity appears to hold in general, it is not true in all cases. The fast ice has a very smooth surface which lowers the autocorrelation and makes it appear as open water in the assessment by the algorithm. Another problem arises over open water, where local wind gusts may induce surface patterns that increase the autocorrelation. It results in the open water being misinterpreted as ice. Homogenous wind fields are normally handled without any problem because they do not generate the same type of small-scale features.

The accuracy of the algorithm is evaluated with ice charts used as reference data, and shown to be slightly better over open water than over sea ice. Overall, the root-mean-square error is less than 7 percentage points for a uniform distribution of ice concentration. The detailed auto-

correlation statistics presented in the paper may be useful for future work on ice concentration and classification with SAR data in the Baltic Sea.

6.2 Paper B

Paper B presents a hybrid sea ice drift algorithm which combines an areal tracking technique with feature-based matching. The paper introduces new methods and ideas on how tracking of sea ice with satellite imagery can be improved. Furthermore, much focus is laid on the optimization of the internal parameters of the algorithm, as the large impact of these internal settings is clearly shown in the analysis. It is shown that the accuracy of the algorithm varies by up to 50% depending on the internal settings. The presented results from the parametric optimization are believed to be applicable to other ice drift algorithms that for instance also use a hierarchic, pyramidal processing approach to iteratively obtain the drift at finer scale.

The algorithm uses subimages from two full-scale images to measure the drift and one drift vector is obtained for each such pair of subimages. It is clear that the size of a subimage sets, on one hand, the spatial resolution of the measured motion field, and on the other hand, the maximum range of measurable drift (at the initial processing stage). The paper suggests a method where one subimage is matched against many in order to overcome this issue. Moreover, a filtering method is presented for how the draft motion field is inherited to the next processing level. The pack ice is often subject to rotation which will lower the cross-correlation and yield uncertain measurements. This is solved by searching for rotation in case of low correlation. The rotation is determined by utilizing the Fourier-Mellin log-polar transform.

The method evaluated for feature-based matching is based on previous work on feature tracking. However, image segmentation is a prerequisite for feature tracking in order to detect floe boundaries. The segmentation is based on intensity thresholding. A special method for threshold selection is presented which is suited for the intensity distributions typically found in SAR images in the marginal ice zone. Furthermore, a novel method is introduced on how to deal with aggregated floes.

6.3 Paper C

The ice drift algorithm presented in paper B is applied in this paper and the retrieved drift is compared to model data. A set of Envisat Wide Swath images from two weeks in April 2011 was acquired over the Fram Strait in the northern Greenland Sea and processed by the algorithm. Low-correlation measurements of the drift were filtered out to obtain reliable motion data. The result is compared to model data from the operational ocean circulation model HIROMB (see section 5.2).

Paper C demonstrates some of the weak points of the ice-ocean model which would benefit from further development. For instance, it is observed that a large section of fast ice along the Greenlandic coast has a major effect on the ice motion of the surrounding ice. The model does not take this effect into account, simply because fast ice is not parameterized well enough and therefore has been switched off. The need to improve fast ice parameterization is therefore concluded. Other deficiencies of the model include overestimation of the ice drift, attributable to underestimated ice thickness, and misaligned drift direction. The latter cannot be explained by the underestimated ice thickness. The reason to the directional offset is thus subject to further investigation.

6.4 Paper D

Paper D considers recently launched SAR missions and evaluates their usefulness for operational sea ice monitoring in the Baltic Sea. The study compares backscatter signatures from L-band data from ALOS PALSAR, C-band data from RADARSAT-2 and ENVISAT ASAR, and X-band data from TerraSAR-X. Further details of the sensors are presented in section 3.1. The major conclusion of the study is that the information content in L-band SAR images is complementary to the information content in the traditionally used C-band SAR data, whereas C- and X-band images are to a high degree equivalent in terms of information content. It is observed that co-polarised L-band images facilitate detection of ridges or ridge clusters and other ice structures, and are less sensitive to wet snow in relation to the higher frequency bands. Continuing with cross-polarisation data, it is established that HV-polarisation is useful for separation between sea ice and wind-roughened open water. The results of this study are specifically important with respect to future missions such as ALOS-2 [126].

6.5 Paper E

This paper demonstrates the capability of InSAR for mapping of fast ice deformation at X-band, and investigates how fast ice properties and dynamics can be assessed from interferograms and auxiliary sources of information. Two image pairs were acquired with the Cosmo-SkyMed satellite system, each with a temporal baseline of 24 hours, over the same area in the north-east Bay of Bothnia in the winter of 2012. The interferometric coherence is shown to be determined by the temporal coherence. The first interferogram exhibits a low degree of coherence, which may be attributed to a temperature increase to values above zero, relatively large ice movement and snowfall. Fringes indicate large deformation closer to the fast ice edge, where the drifting pack ice is believed to exert pressure on the fast ice. The second interferogram has a high degree of coherence overall. The coherence was used to distinguish regions within the fast

ice, and possible sources of the coherence variations are discussed. Deformation appears to be stronger around leads and rocky islands. The study lists a few possible explanations to the fringe patterns and assesses their likeliness. Specifically, thermal ice expansion and grounded ice ridges are probable causes to observed deformations.

Chapter 7

Conclusion and future research

The scope of this thesis extends from SAR observations of sea ice concentration and drift to investigation of the potential capabilities of new SAR sensors for operational sea ice monitoring and InSAR measurements of land-fast ice. To begin with, it has been shown that the high-resolution imaging capabilities of spaceborne SAR enable detailed measurements of ice concentration and drift.

The ice concentration algorithm was developed for use with single-polarized one-channel ScanSAR images. This imaging mode is commonly used for routine observations and the preferred mode by the ice services. It is foreseen, however, that dual-polarisation ScanSAR will replace the use of single-polarised mode. The future Sentinel-1 SAR satellite, planned for launch in 2014, will provide dual-polarisation in ScanSAR mode [127, 28]. This is already the case for RADARSAT-2 with its dual-polarised wide beam mode. An important research topic for the future is thus the utilization of dual-polarisation data. The HH channel is advantageous for assessing certain ice properties, whereas the HV channel is the best choice for other properties. For instance, the ice type can easier be determined from co-polarised data and the location of the ice edge from the cross-polarised data. The cross-polarized return is however much weaker, which implies hard constraints on the noise level. If the information from the HH and HV channels can be combined in an optimal way, it is possible that future ice concentration algorithms would be able to compete with visual classification by an experienced ice analyst. Using single-polarisation data only, it is overly difficult to create a computer program that can match the classification made by an experienced ice analyst.

Over the last three decades, there has been an ongoing development of methods for retrieval of ice drift from sequential SAR images. The battlefront of today's algorithms is on getting more reliable measurements in difficult areas such as the marginal ice zone and to achieve high performance also during the melting period. In this thesis, it has been shown that feature tracking can be used in combination with areal tracking in order to improve the results in the marginal ice zone. The presented procedure does not provide a full solution to the tracking

problem in the marginal ice zone, but the basic principle to combine feature tracking and areal tracking is pointed out as a convincing way forward.

With the increasing computer capacity, more complex techniques can be used to track the ice drift. It would be possible, for instance, to implement a procedure where candidate solutions are kept in the system until they can be resolved. Suppose that one subimage is correlated with another, and two candidate solutions appear with similar correlation/likelihood. One method is then to filter them with normalized cross-correlation [108]. Another option, however, would be to keep both solutions and process them recursively. Once a solution is approved (e.g. by reaching acceptable correlation at a later processing stage with finer resolution and smaller subimages, or by finding a solution in good agreement with the neighbouring solutions), it will be selected and the other candidate solution will be disregarded.

Feature-based matching of sea ice will likely develop further. The feature tracking technique proposed by Das Peddala [128], and applied in paper C, is found to perform well for tracking of ice floe boundaries. It is, however, based on a priori knowledge of floe boundaries. The key to well-functioning feature-based matching is thus to have a reliable image segmentation method that is able to identify individual ice floes with high accuracy. A simple method was proposed in paper C, based on intensity thresholding, which can be used for further development (for instance in combination with edge detection). A frequent segmentation problem occurs in regions of high ice concentration, typically above 70–80%, where the ice floes are densely packed. When floes start to merge with each other in all directions, it is very difficult to separate them by automatic means. A method has been proposed in paper C on how to deal with aggregated floes, but it must be noted that the method performs best at medium ice concentrations.

It is foreseen that a combined sea ice concentration/drift analysis of a series of (at least two) SAR scenes would give an improved end-product. The reasoning is that diverging ice is an indication of decreasing ice concentration whereas converging ice may be linked to an increase in ice concentration or deformation. By relating these processes to each other via a simple flow model, it would be possible to obtain a consistent solution to the ice motion and concentration where the estimates of the different parameters benefit from each other.

There is a need to improve modelling of sea ice dynamics. While paper C indicates that the general drift patterns can be modelled reasonably well by HIROMB in the Fram Strait region, the magnitude of the drift and the drift direction are off. One part of the solution is to gather more observational data of sea ice thickness for assimilation into models, which is a key parameter and a major uncertainty. Another part that should be considered is the fast ice, which is an intricate matter for modelers. Here it is possible that further studies of fast ice with interferometric SAR can provide valuable input to the modelling community regarding fast ice strength. As a third step towards improved modelling, the impact of the atmospheric forcing data needs to be assessed. Atmospheric forcing data with coarse spatial resolution has proved

to have a negative influence on the accuracy of the modelled ice drift in a coupled ice-ocean model [129].

Bibliography

[1] G. J. Laidler, J. D. Ford, W. A. Gough, T. Ikummaq, A. S. Gagnon, S. Kowal, K. Qrunnut, and C. Irngaut, "Travelling and hunting in a changing Arctic: assessing Inuit vulnerability to sea ice change in Igloolik, Nunavut," *Climatic Change*, vol. 94, no. 3-4, pp. 363–397, 2009.

[2] M. Gosselin, M. Levasseur, P. A. Wheeler, R. A. Horner, and B. C. Booth, "New measurements of phytoplankton and ice algal production in the Arctic Ocean," *Deep Sea Research Part II: Topical Studies in Oceanography*, vol. 44, no. 8, pp. 1623–1644, 1997.

[3] O. M. Johannessen, V. Y. Alexandrov, I. Y. Frolov, L. P. Bobylev, S. Sandven, L. H. Pettersson, K. Kloster, N. G. Babich, Y. U. Mironov, and V. G. Smirnov, *Remote Ssensing of Sea Ice in the Northern Sea Route: Studies and Applications*. Springer, 2007.

[4] S. M. Bhandari, M. K. Dash, N. K. Vyas, N. Khare, and P. C. Pandey, *Microwave Remote Sensing of Ice in the Antarctic Region from OCEANSAT-1*, ch. 22, pp. 423–451. New Delhi, India: A.P.H. Publishing Corporation, 2002.

[5] J. Comiso and H. Zwally, "Antarctic sea ice concentrations inferred from Nimbus 5 ESMR and Landsat imagery," *Journal of Geophysical Research*, vol. 87, no. C8, pp. 5836–5844, 1982.

[6] D. L. Evans, W. Alpers, A. Cazenave, C. Elachi, T. Farr, D. Glackin, B. Holt, L. Jones, W. T. Liu, and W. McCandless, "Seasat – A 25-year legacy of success," *Remote Sensing of Environment*, vol. 94, no. 3, pp. 384–404, 2005.

[7] L.-L. Fu and B. Holt, "Seasat views oceans and sea ice with synthetic aperture radar," tech. rep., Jet Propulsion Laboratory, Pasadena, CA, 1982.

[8] Danish Meteorological Institute, *Nautisk Meteorologisk Aarbog*. 1893–1961.

[9] J. Karvonen, "Tracking the motion of recognizable sea-ice objects from coastal radar image sequences," *Annals of Glaciology*, vol. 54, no. 62, p. 41, 2013.

[10] M. L. Druckenmiller, H. Eicken, M. A. Johnson, D. J. Pringle, and C. C. Williams, "Toward an integrated coastal sea-ice observatory: System components and a case study at Barrow, Alaska," *Cold Regions Science and Technology*, vol. 56, no. 2, pp. 61–72, 2009.

[11] J. Groves and W. Stringer, "The use of AVHRR thermal infrared imagery to determine sea ice thickness within the Chukchi polynya," *Arctic*, vol. 44, pp. 130–139, 1991.

[12] C. J. Donlon, M. Martin, J. Stark, J. Roberts-Jones, E. Fiedler, and W. Wimmer, "The operational sea surface temperature and sea ice analysis (OSTIA) system," *Remote Sensing of Environment*, vol. 116, pp. 140–158, 2012.

[13] S.-K. Min, X. Zhang, F. W. Zwiers, and T. Agnew, "Human influence on Arctic sea ice detectable from early 1990s onwards," *Geophysical Research Letters*, vol. 35, no. 21, p. L21701, 2008.

[14] F. Fetterer, K. Knowles, W. Meier, and M. Savoie, *Sea Ice Index: Northern Hemisphere, 1978-2013*. Boulder, Colorado, USA: National Snow and Ice Data Center, 2002.

[15] F. D. Carsey (Ed.), *Microwave Remote Sensing of Sea Ice*. Washington, DC: American Geophysical Union, 1992.

[16] D. J. Cavalieri, P. Gloersen, and W. J. Campbell, "Determination of sea ice parameters with the NIMBUS 7 SMMR," *Journal of Geophysical Research*, vol. 89, no. D4, pp. 5355–5369, 1984.

[17] N. J. Willis, *Bistatic Radar*. Raleigh, NC: SciTech Publishing Inc., 2nd ed., 2005.

[18] The Institute of Electrical and Electronics Engineers, *IEEE Standard Letter Designations for Radar-Frequency Bands*, 1984.

[19] M. A. Richards, J. A. Scheer, J. Scheer, and W. A. Holm, *Basic principles*, vol. 1 of *Principles of modern radar*. Raleigh, NC: SciTech Publishing Inc., 2010.

[20] R. Sullivan, *Radar Foundations for Imaging and Advanced Concepts*. Raleigh, NC: SciTech Publishing Inc., 2004.

[21] P. Z. Peebles, *Radar Principles*. New York, NY: John Wiley & Sons, Inc., 1998.

[22] F. T. Ulaby, R. K. Moore, and A. K. Fung, *Microwave Remote Sensing Active and Passive Vol. II: Radar Remote Sensing and Surface Scattering and Emission Theory*. Artech House, Norwood MA, Artech House.

[23] W. G. Carrara, R. S. Goodman, and R. M. Majewski, *Spotlight Synthetic Aperture Radar - Signal Processing Algorithms*. Norwood, MA: Artech House, 1995.

[24] W. Melvin and J. Scheer, *Advanced Techniques*, vol. 2 of *Principles of Modern Radar*. Edison, NJ: SciTech Publishing Inc., 2013.

[25] R. Bamler and M. Eineder, "ScanSAR processing using standard high precision SAR algorithms," *IEEE Transactions on Geoscience and Remote Sensing*, vol. 34, no. 1, pp. 212–218, 1996.

[26] K. Tomiyasu, "Conceptual performance of a satellite borne, wide swath synthetic aperture radar," *IEEE Transactions on Geoscience and Remote Sensing*, vol. 19, no. 2, pp. 108–116, 1981.

[27] F. De Zan and A. M. Guarnieri, "TOPSAR: Terrain observation by progressive scans," *IEEE Transactions on Geoscience and Remote Sensing*, vol. 44, no. 9, pp. 2352–2360, 2006.

[28] R. Torres, P. Snoeij, D. Geudtner, D. Bibby, M. Davidson, E. Attema, P. Potin, B. Rommen, N. Floury, and M. Brown, "GMES Sentinel-1 mission," *Remote Sensing of Environment*, vol. 120, pp. 9–24, 2012.

[29] C. Oliver and S. Quegan, *Understanding Synthetic Aperture Radar Images*. Norwood, MA: Artech House, 1998.

[30] C. Elachi, *Spaceborne Radar Remote Sensing: Applications and Techniques*. New York, NY: IEEE Press, 2 ed., 1988.

[31] D. W. Hawkins, *Synthetic Aperture Imaging Algorithms: With Application to Wide Bandwidth Sonar*. Ph.D. thesis, University of Canterbury, 1996.

[32] R. Bamler and P. Hartl, "Synthetic aperture radar interferometry," *Inverse problems*, vol. 14, no. 4, p. R1, 1998.

[33] H. A. Zebker and R. M. Goldstein, "Topographic mapping from interferometric synthetic aperture radar observations," *Journal of Geophysical Research: Solid Earth*, vol. 91, no. B5, pp. 4993–4999, 1986.

[34] R. M. Goldstein, H. A. Zebker, and C. L. Werner, "Satellite radar interferometry: Two-dimensional phase unwrapping," *Radio Science*, vol. 23, no. 4, pp. 713–720, 1988.

[35] D. Massonnet and K. L. Feigl, "Radar interferometry and its application to changes in the Earth's surface," *Reviews of Geophysics*, vol. 36, no. 4, pp. 441–500, 1998.

[36] X. Zhou, N.-B. Chang, and S. Li, "Applications of SAR interferometry in earth and environmental science research," *Sensors*, vol. 9, no. 3, pp. 1876–1912, 2009.

[37] P. Dammert, *Spaceborne SAR Interferometry: Theory and Applications*. Ph.D. thesis, Chalmers University of Technology, 1999.

[38] Q. Lin, J. F. Vesecky, and H. A. Zebker, "New approaches in interferometric SAR data processing," *IEEE Transactions on Geoscience and Remote Sensing*, vol. 30, no. 3, pp. 560–567, 1992.

[39] D. Derauw, "DInSAR and coherence tracking applied to glaciology: The example of Shirase Glacier," in *Proceedings of FRINGE99 workshop*, 1999.

[40] T. Strozzi, A. Luckman, T. Murray, U. Wegmuller, and C. L. Werner, "Glacier motion estimation using SAR offset-tracking procedures," *IEEE Transactions on Geoscience and Remote Sensing*, vol. 40, no. 11, pp. 2384–2391, 2002.

[41] H. A. Zebker, P. A. Rosen, and S. Hensley, "Atmospheric effects in interferometric synthetic aperture radar surface deformation and topographic maps," *Journal of Geophysical Research*, vol. 102, no. B4, pp. 7547–7563, 1997.

[42] M. Costantini, "A novel phase unwrapping method based on network programming," *IEEE Transactions on Geoscience and Remote Sensing*, vol. 36, no. 3, pp. 813–821, 1998.

[43] W. Xu and I. Cumming, "A region-growing algorithm for InSAR phase unwrapping," *IEEE Transactions on Geoscience and Remote Sensing*, vol. 37, no. 1, pp. 124–134, 1999.

[44] S. Li, C. Benson, R. Gens, and C. Lingle, "Motion patterns of Nabesna Glacier (Alaska) revealed by interferometric SAR techniques," *Remote Sensing of Environment*, vol. 112, no. 9, pp. 3628–3638, 2008.

[45] F. Gatelli, A. M. Guamieri, F. Parizzi, P. Pasquali, C. Prati, and F. Rocca, "The wavenumber shift in SAR interferometry," *IEEE Transactions on Geoscience and Remote Sensing*, vol. 32, no. 4, pp. 855–865, 1994.

[46] L. M. H. Ulander, A. Carlström, and J. Askne, "ERS-1 SAR backscatter from nilas and young ice during freeze-up," *EARSeL Advances in Remote Sensing*, vol. 3, no. 2, pp. 1–8, 1994.

[47] L. M. H. Ulander, A. Carlström, and J. Askne, "Effect of frost flowers, rough saline snow and slush on the ERS-1 SAR backscatter of thin Arctic sea-ice," *International Journal of Remote Sensing*, vol. 16, no. 17, pp. 3287–3305, 1995.

[48] W. Dierking, A. Carlström, and L. M. H. Ulander, "The effect of inhomogeneous roughness on radar backscattering from slightly deformed sea ice," *IEEE Transactions on Geoscience and Remote Sensing*, vol. 35, no. 1, pp. 147–159, 1997.

[49] M. Mäkynen, *Investigation of the Microwave Signatures of the Baltic Sea Ice.* Ph.D. thesis, Helsinki University of Technology, 2007.

[50] L. M. H. Ulander, *Radar Remote Sensing of Sea Ice: Measurements and Theory.* Ph.D. thesis, Chalmers University of Technology, 1991.

[51] A. Carlström and L. M. H. Ulander, "C-band backscatter signatures of old sea ice in the central Arctic during freeze-up," *IEEE Transactions on Geoscience and Remote Sensing*, vol. 31, no. 4, pp. 819–829, 1993.

[52] A. Carlström, *Modelling Microwave Backscattering from Sea Ice for Synthetic-Aperture Radar Applications.* Ph.D. thesis, Chalmers University of Technology, 1995.

[53] M. R. Drinkwater, R. Kwok, D. Winebrenner, and E. Rignot, "Multifrequency polarimetric synthetic aperture radar observations of sea ice," *Journal of Geophysical Research*, vol. 96, no. C11, pp. 679–698, 1991.

[54] E. R. Stofan, D. L. Evans, C. Schmullius, B. Holt, J. J. Plaut, J. van Zyl, S. D. Wall, and J. Way, "Overview of results of spaceborne imaging radar-C, X-band synthetic aperture radar (SIR-C/X-SAR)," *IEEE Transactions on Geoscience and Remote Sensing*, vol. 33, no. 4, pp. 817–828, 1995.

[55] L. E. B. Eriksson, M. R. Drinkwater, B. Holt, E. Valjavek, and O. Nortier, "SIR-C polarimetric radar results from the Weddell Sea, Antarctica," in *Proceedings of the IEEE International Geoscience and Remote Sensing Symposium (IGARSS'98)*, vol. 4, pp. 2222–2224, IEEE, 1998.

[56] M.-A. Moen, A. Doulgeris, S. Anfinsen, A. Renner, N. Hughes, S. Gerland, and T. Eltoft, "Comparison of feature based segmentation of full polarimetric SAR satellite sea ice images with manually drawn ice charts," *The Cryosphere*, vol. 7, no. 6, pp. 1693–1705, 2013.

[57] W. Dierking, H. Skriver, and P. Gudmandsen, "On the improvement of sea ice classification by means of radar polarimetry," in *Proceedings of the 23rd EARSeL Symposium on Remote Sensing in Transition*, pp. 203–209, R. Goossens, 2004.

[58] K. Nakamura, H. Wakabayashi, K. Naoki, F. Nishio, T. Moriyama, and S. Uratsuka, "Observation of sea-ice thickness in the sea of Okhotsk by using dual-frequency and fully polarimetric airborne SAR (pi-SAR) data," *IEEE Transactions on Geoscience and Remote Sensing*, vol. 43, no. 11, pp. 2460–2469, 2005.

[59] K. Nakamura, H. Wakabayashi, S. Uto, S. Ushio, and F. Nishio, "Observation of sea-ice thickness using ENVISAT data from Lützow-Holm Bay, East Antarctica," *IEEE Geoscience and Remote Sensing Letters*, vol. 6, no. 2, pp. 277–281, 2009.

[60] D. Bäck, B. Holt, and R. Kwok, "Analysis of C-band polarimetric signatures of Arctic lead ice using data from AIRSAR and RADARSAT-1," in *Proceedings of the IEEE International Geoscience and Remote Sensing Symposium (IGARSS'08)*, vol. 5, pp. 184–187, IEEE, 2008.

[61] D. Winebrenner, L. Farmer, and I. Joughin, "On the response of polarimetric synthetic aperture radar signatures at 24-cm wavelength to sea ice thickness in Arctic leads," *Radio Science*, vol. 30, no. 2, pp. 373–402, 1995.

[62] B. B. Thomsen, S. Nghiem, and R. Kwok, "Polarimetric C-band SAR observations of sea ice in the Greenland Sea," in *Proceedings of the International Geoscience and Remote Sensing Symposium (IGARSS'98)*, vol. 5, pp. 2502–2504, IEEE, 1998.

[63] S. R. Cloude and E. Pottier, "A review of target decomposition theorems in radar polarimetry," *IEEE Transactions on Geoscience and Remote Sensing*, vol. 34, no. 2, pp. 498–518, 1996.

[64] J.-S. Lee and E. Pottier, *Polarimetric Radar Imaging: From Basics to Applications*. CRC Press, Taylor & Francis Group, 2009.

[65] B. Scheuchl, *Sea Ice Monitoring using Spaceborne Multi-Polarization and Polarimetric SAR Imagery*. Ph.D. thesis, University of British Columbia, 2006.

[66] H. Wakabayashi, T. Matsuoka, K. Nakamura, and F. Nishio, "Polarimetric characteristics of sea ice in the sea of Okhotsk observed by airborne L-band SAR," *IEEE Transactions on Geoscience and Remote Sensing*, vol. 42, no. 11, pp. 2412–2425, 2004.

[67] J. P. Gill and J. J. Yackel, "Evaluation of C-band SAR polarimetric parameters for discrimination of first-year sea ice types," *Canadian Journal of Remote Sensing*, vol. 38, no. 03, pp. 306–323, 2012.

[68] H. J. Kramer, *Observation of the Earth and Its Environment: Survey of Missions and Sensors*. Berlin, Germany: Springer-Verlag, 4th ed., 2002.

[69] B. R. Ramsay, L. Weir, K. Wilson, and M. Arkett, "Early results of the use of RADARSAT ScanSAR data in the Canadian Ice Service," in *Remote Sensing of the Polar Environments*, vol. 391, p. 95, ESA, 1996.

[70] B. Scheuchl, D. Flett, R. Caves, and I. Cumming, "Potential of RADARSAT-2 data for operational sea ice monitoring," *Canadian Journal of Remote Sensing*, vol. 30, no. 3, pp. 448–461, 2004.

[71] J. Louet and S. Bruzzi, "Envisat mission and system," in *Proceedings of the International Geoscience and Remote Sensing Symposium (IGARSS'99)*, vol. 3, pp. 1680–1682, IEEE, 1999.

[72] F. Covello, F. Battazza, A. Coletta, E. Lopinto, C. Fiorentino, L. Pietranera, G. Valentini, and S. Zoffoli, "COSMO-SkyMed an existing opportunity for observing the Earth," *Journal of Geodynamics*, vol. 49, no. 3, pp. 171–180, 2010.

[73] L. Morena, K. James, and J. Beck, "An introduction to the RADARSAT-2 mission," *Canadian Journal of Remote Sensing*, vol. 30, no. 3, pp. 221–234, 2004.

[74] A. Berg, L. E. B. Eriksson, K. Borenäs, and H. Lindh, "Observations and analysis of sea ice motion with the ice buoy DRIVA during the 2010 spring field campaign in the Bay of Bothnia," Tech. Rep. 7, Dept. of Earth and Space Sciences, Chalmers University of Technology, Gothenburg, Sweden, 2011.

[75] J. S. Löfgren, *Local Sea Level Observations Using Reflected GNSS Signals*. Ph.D. thesis, Chalmers University of Technology, 2014.

[76] C. Deser and H. Teng, "Evolution of Arctic sea ice concentration trends and the role of atmospheric circulation forcing, 1979-2007," *Geophysical Research Letters*, vol. 35, L02504, no. 2, 2008.

[77] D. J. Cavalieri, P. Gloersen, C. L. Parkinson, J. C. Comiso, and H. J. Zwally, "Observed hemispheric asymmetry in global sea ice changes," *Science*, vol. 278, no. 5340, pp. 1104–1106, 1997.

[78] J. Askne, L. M. H. Ulander, and D. Birkeland, "Accuracy of ice concentration derived from ERS-1 SAR images during the late melt period in the Arctic," *EARSeL Advances in Remote Sensing*, vol. 3, no. 2, pp. 44–49, 1994.

[79] M. Fily and D. A. Rothrock, "Extracting sea ice data from satellite SAR imagery," *IEEE Transactions on Geoscience and Remote Sensing*, vol. 24, no. 6, pp. 849–854, 1986.

[80] M. Mäkynen and M. Hallikainen, "Investigation of C- and X-band backscattering signatures of Baltic Sea ice," *International Journal of Remote Sensing*, vol. 25, no. 11, pp. 2061–2086, 2004.

[81] M. Pettersson, *Contribution to Wideband SAR Space-time Processing, and Radar Remote Sensing of Sea Ice*. Ph.D. thesis, Chalmers University of Technology, 2000.

[82] S. T. Dokken, *Sea Ice and Ocean Environmental Applications of Spaceborne SAR*. Ph.D. thesis, Chalmers University of Technology, 2000.

[83] S. Sandven, O. Dalen, M. Lundhaug, K. Kloster, V. Y. Alexandrov, and L. Zaitsev, "Sea ice investigations in the Laptev Sea area in late summer using SAR data: Ice and icebergs," *Canadian Journal of Remote Sensing*, vol. 27, no. 5, pp. 502–516, 2001.

[84] D. A. Clausi, "Comparison and fusion of co-occurrence, Gabor and MRF texture features for classification of SAR sea-ice imagery," *Atmosphere-Ocean*, vol. 39, no. 3, pp. 183–194, 2001.

[85] J. A. Nystuen and F. W. Garcia, "Sea ice classification using SAR backscatter statistics," *IEEE Transactions on Geoscience and Remote Sensing*, vol. 30, no. 3, pp. 502–509, 1992.

[86] L. K. Soh and C. Tsatsoulis, "Texture analysis of SAR sea ice imagery using gray level co-occurrence matrices," *IEEE Transactions on Geoscience and Remote Sensing*, vol. 37, no. 2, pp. 780–795, 1999.

[87] H. Deng and D. A. Clausi, "Unsupervised segmentation of synthetic aperture radar sea ice imagery using a novel Markov random field model," *IEEE Transactions on Geoscience and Remote Sensing*, vol. 43, no. 3, pp. 528–538, 2005.

[88] M. Similä, "SAR image segmentation by a two-scale contextual classifier," *Image and Signal Processing for Remote Sensing*, vol. 2315, pp. 434–443, 1994.

[89] J. Karvonen, M. Similä, and M. Mäkynen, "Open water detection from Baltic sea ice Radarsat-1 SAR imagery," *IEEE Geoscience and Remote Sensing Letters*, vol. 2, no. 3, pp. 275–279, 2005.

[90] J. Karvonen, "Baltic sea ice concentration estimation based on C-band HH-polarized SAR data," *IEEE Journal of Selected Topics in Applied Earth Observations and Remote Sensing*, vol. 5, no. 6, pp. 1874–1884, 2012.

[91] J. Karvonen, "Baltic sea ice concentration estimation based on C-band dual-polarized SAR data," 2014. Accepted for publication in IEEE Transactions on Geoscience and Remote Sensing.

[92] H. Wakabayashi and S. Sakai, "Sea ice area detection in the sea of Okhotsk using PALSAR polarimetric data," in *Proceedings of the 3rd International Asia-Pacific Conference on Synthetic Aperture Radar (APSAR)*, pp. 1–4, IEEE, 2011.

[93] D. Belliveau, G. Bugden, and S. Melrose, "Measurement of sea ice motion using bottom mounted Acoustic Doppler Current Profilers," *Sea Technology*, vol. 30, pp. 10–12, 1989.

[94] R. Birch, D. Fissel, H. Melling, K. Vaudrey, W. Lamb, K. Schaudt, and J. Heideman, "Ice-profiling sonar," *Sea Technology*, vol. 41, no. 8, pp. 48–54, 2000.

[95] R. Kwok, J. C. Curlander, R. McConnell, and S. S. Pang, "An ice-motion tracking system at the Alaska SAR facility," *IEEE Journal of Oceanic Engineering*, vol. 15, no. 1, pp. 44–54, 1990.

[96] R. Kwok, A. Schweiger, D. Rothrock, S. Pang, and C. Kottmeier, "Sea ice motion from satellite passive microwave imagery assessed with ERS SAR and buoy motions," *Journal of Geophysical Research*, vol. 103, no. C4, pp. 8191–8214, 1998.

[97] Y. Sun, *SAR Remote Sensing of Sea Ice: Towards Automatic Extraction of Geophysical Information*. Ph.D. thesis, Chalmers University of Technology, 1995.

[98] T. Martin and E. Augstein, "Large-scale drift of Arctic sea ice retrieved from passive microwave satellite data," *Journal of Geophysical Research: Oceans*, vol. 105, no. C4, pp. 8775–8788, 2000.

[99] F. Leberl, M. Bryan, C. Elachi, T. Farr, and W. Campbell, "Mapping of sea ice and measurement of its drift using aircraft synthetic aperture radar images," *Journal of Geophysical Research*, vol. 84, no. C4, pp. 1827–1835, 1979.

[100] R. Hall and D. Rothrock, "Sea ice displacement from Seasat synthetic aperture radar," *Journal of Geophysical Research*, vol. 86, no. C11, pp. 11078–11082, 1981.

[101] M. Fily and D. Rothrock, "Sea ice tracking by nested correlations," *IEEE Transactions on Geoscience and Remote Sensing*, vol. GE-25, no. 5, pp. 570–580, 1987.

[102] K. Kloster, H. Flesche, and O. M. Johannessen, "Ice motion from airborne SAR and satellite imagery," *Advances in Space Research*, vol. 12, no. 7, pp. 149–153, 1992.

[103] S. Sandven, O. M. Johannessen, M. W. Miles, L. H. Pettersson, and K. Kloster, "Barents Sea seasonal ice zone features and processes from ERS 1 synthetic aperture radar: Seasonal Ice Zone Experiment 1992," *Journal of Geophysical Research: Oceans*, vol. 104, no. C7, pp. 15843–15857, 1999.

[104] C. Kuglin and D. Hines, "The phase correlation image alignment method," in *Proceedings of International Conference on Cybernetics and Society*, pp. 163–165, 1975.

[105] Y. Sun, "Automatic ice motion retrieval from ERS-1 SAR images using the optical flow method," *International Journal of Remote Sensing*, vol. 17, no. 11, pp. 2059 – 2087, 1996.

[106] R. Ninnis, W. Emery, and M. Collins, "Automated extraction of pack ice motion from advanced very high resolution radiometer imagery," *Journal of Geophysical Research*, vol. 91, no. C9, pp. 10725–10734, 1986.

[107] R. Michel and E. Rignot, "Flow of Moreno Glaciar, Argentina, from repeat-pass Shuttle Imaging Radar images: Comparison of the phase correlation method with radar interferometry," *Journal of Glaciology*, vol. 45, no. 149, pp. 93–100, 1999.

[108] M. Thomas, C. A. Geiger, and C. Kambhamettu, "High resolution (400 m) motion characterization of sea ice using ERS-1 SAR imagery," *Cold Regions Science and Technology*, vol. 52, no. 2, pp. 207–223, 2008.

[109] T. Hollands, *Motion Tracking of Sea Ice with SAR Satellite Data*. Ph.D. thesis, Universität Bremen, 2012.

[110] M. Leppäranta, *The Drift of Sea Ice*. Springer-Verlag Berlin Heidelberg, 2011.

[111] J. L. Bamber and A. J. Payne, *Mass Balance of the Cryosphere*. Cambridge, UK: Cambridge University Press, 2004.

[112] R. E. Moritz and H. L. Stern, *Relationships Between Geostrophic Winds, Ice Strain Rates and the Piecewise Rigid Motions of Pack Ice*, vol. 94 of *Solid Mechanics and Its Applications*, ch. 28, pp. 335–348. Springer Netherlands, 2001.

[113] C. K. Rheem, H. Yamaguchi, and H. Kato, "Distributed mass/discrete floe model for pack ice rheology computation," *Journal of Marine Science and Technology*, vol. 2, no. 2, pp. 101–121, 1997.

[114] R. G. Barry, *Cryosphere Models*, pp. 1704–1718. Encyclopedia of Complexity and Systems Science, Springer, 2009.

[115] W. D. Hibler III, "A dynamic thermodynamic sea ice model," *Journal of Physical Oceanography*, no. 4, pp. 815–846, 1979.

[116] E. Kleine and S. Sklyar, "Mathematical features of Hibler's model of large-scale sea-ice dynamics," *Deutsche Hydrografische Zeitschrift*, vol. 47, no. 3, pp. 179–230, 1995.

[117] R. Timmermann, A. Beckmann, and H. Hellmer, "Simulations of ice-ocean dynamics in the Weddell Sea 1. Model configuration and validation," *Journal of Geophysical Research: Oceans*, vol. 107, no. C3, pp. 1–11, 2002.

[118] J.-O. Wolff, E. Maier-Reimer, and S. Legutke, "The Hamburg ocean primitive equation model," Tech. Rep. 13, DKRZ, Hamburg, Germany, 1997.

[119] J. M. Oberhuber, "Simulation of the Atlantic circulation with a coupled sea ice-mixed layer-isopycnal general circulation model. Part I: Model description," *Journal of Physical Oceanography*, vol. 23, no. 5, pp. 808–829, 1993.

[120] W. D. Hibler III, "Modeling a variable thickness sea ice cover," *Monthly weather review*, vol. 108, no. 12, pp. 1943–1973, 1980.

[121] J. Haapala and M. Leppäranta, "Simulating the Baltic Sea ice season with a coupled ice-ocean model," *Tellus A*, vol. 48, no. 5, pp. 622–643, 1996.

[122] L. Funkquist and E. Kleine, "An introduction to HIROMB, an operational baroclinic model for the Baltic Sea," Tech. Rep. 37, Swedish Meteorological and Hydrological Institute, Sweden, 2007.

[123] K. Bryan, "A numerical method for the study of the circulation of the world ocean," *Journal of Computational Physics*, vol. 4, no. 3, pp. 347–376, 1969.

[124] T. Wilhelmsson, *Parallelization of the HIROMB Ocean Model*. Licentiate thesis, Royal Institute of Technology, Stockholm, Sweden, 2002.

[125] A. J. Semtner Jr, "A model for the thermodynamic growth of sea ice in numerical investigations of climate," *Journal of Physical Oceanography*, vol. 6, no. 3, pp. 379–389, 1976.

[126] Y. Kankaku, Y. Osawa, S. Suzuki, and T. Watanabe, "The overview of the L-band SAR onboard ALOS-2," in *Proceedings of Progress in Electromagnetics Research Symposium*, 2009.

[127] E. Attema, P. Bargellini, P. Edwards, G. Levrini, S. Lokas, L. Moeller, B. Rosich-Tell, P. Secchi, R. Torres, and M. Davidson, "Sentinel-1 — the radar mission for GMES operational land and sea services," *ESA bulletin*, vol. 131, pp. 10–17, 2007.

[128] S. Das Peddada and R. McDevitt, "Least average residual algorithm (LARA) for tracking the motion of Arctic sea ice," *IEEE Transactions on Geoscience and Remote Sensing*, vol. 34, no. 4, pp. 915–926, 1996.

[129] T. Hollands, V. Haid, W. Dierking, R. Timmermann, and L. Ebner, "Sea ice motion and open water area at the Ronne Polynia, Antarctica: Synthetic aperture radar observations versus model results," *Journal of Geophysical Research: Oceans*, vol. 118, pp. 1940–1954, 2013.